University of Nebraska - Lincoln
DigitalCommons@University of Nebraska - Lincoln

Student Research Projects, Dissertations, and Theses - Chemistry Department

Chemistry, Department of

4-2017

Chemical Vapor Deposition of Two-Dimensional Materials and Heterostructures

Alex J. Boson
University of Nebraska-Lincoln, aboson@huskers.unl.edu

Follow this and additional works at: http://digitalcommons.unl.edu/chemistrydiss

Part of the Chemistry Commons

Boson, Alex J., "Chemical Vapor Deposition of Two-Dimensional Materials and Heterostructures" (2017). *Student Research Projects, Dissertations, and Theses - Chemistry Department*. 80.
http://digitalcommons.unl.edu/chemistrydiss/80

This Article is brought to you for free and open access by the Chemistry, Department of at DigitalCommons@University of Nebraska - Lincoln. It has been accepted for inclusion in Student Research Projects, Dissertations, and Theses - Chemistry Department by an authorized administrator of DigitalCommons@University of Nebraska - Lincoln.

Chemical Vapor Deposition of Two-Dimensional Materials and Heterostructures

by

Alex J. Boson

A THESIS

Presented to the Faculty of

The Graduate College at the University of Nebraska

In Partial Fulfillment of Requirements

For the Degree of Master of Science

Major: Chemistry

Under the Supervision of Professor Alexander Sinitskii

Lincoln, Nebraska

April, 2017

CHEMICAL VAPOR DEPOSITION OF TWO-DIMENSIONAL MATERIALS AND HETEROSTRUCTURES

Alex J. Boson, M.S.

University of Nebraska, 2017

Advisor: Alexander Sinitskii

A family of materials similar to graphene are transition metal dichalcogenides (TMDs) which have emerged as an improved alternative. Importantly, each combination of TMD is unique, possessing different properties. Chemical vapor deposition (CVD) has become a popular method to grow TMDs at large scale and in reproducible fashion. Molybdenum disulfide (MoS_2) has been intensely studied at the monolayer due the creation of an indirect band gap but little has been done to investigate few layered structures and as the number of layers change, so do the properties. In this work, CVD is utilized to grow uniform bilayer and trilayer MoS_2 triangular islands and compare few layer islands to their monolayer counterpart. Another TMD, tungsten disulfide (WS_2), also has an indirect band gap at the monolayer. The combination of different two-dimensional (2D) materials has become a new way to achieve different structures with tunable properties. Stacking of 2D materials using van der Waals interactions has already created a pathway to an almost limitless number of combinations. A common combination is graphene and boron nitride because boron nitride has the same structure as graphene and creates an insulated layer with very little charge trapping and surface defects. As a starting point for 2D heterostructures, graphene on top of boron nitride was investigated and found to indeed reduce charge trappings creating a Dirac point closer to zero than other dielectric substrates. With the previous work done using CVD to grow TMDs it was also thought possible to grow MoS_2 on boron nitride to improve the quality and reduce charge trappings from the substrate. The quality of the MoS_2 became improved due to similar lattice structures leading to epitaxial growth along

the boron nitride. Finally, CVD combining the two TMDs studied above was used to create lateral heterostructures. The combination of these two materials creates a theoretically staggered band gap that could lead to controllable electronic or optical properties not yet explored due to the limitations of conventional stacked heterostructures.

Table of Contents

Table of Figures ii
Chapter 1: Molybdenum Disulfide 1
Background 1
Introduction 3
Experimental Procedure 6
Results and Discussion 10
Chapter 2: Tungsten Disulfide 26
Introduction 26
Experimental Procedure 27
Results and Discussion 28
Chapter 3: Heterostructures of 2D materials 39
3.1 Graphene on boron nitride 40
Introduction 40
Experimental Methods 41
Results and Discussion 44
3.2 Molybdenum disulfide on boron nitride 54
Introduction 54
Experimental Procedure 55
Results and Discussion 56
3.3 Molybdenum disulfide/tungsten disulfide 64
Introduction 64
Experimental Procedure 65
Results and Discussion 66
Conclusion and Future Outlook 74
References 76

Table of Figures

Figure 1 CVD growth of MoS_2 islands with different thicknesses. (a) Scheme of the CVD setup. (b) Experimental parameters for growing MoS_2 with a different number of layers. T_F represents the temperature of the furnace and T_{HP} represents the temperature of the hotplate. Arrows indicate the time when T_{HP} is increased and held constant.....................8

Figure 2 Different shapes of MoS_2 islands in the form of stars (a), hexagons (b), merging islands (c) and uniform triangles (d). Scale bar is the same for all images. 12

Figure 3 Optical photograph of a Si/SiO_2 substrate with monolayer (1L), bilayer (2L) and trilayer (3L) MoS_2 islands with single nucleation sites. 16

Figure 4 Characterization of MoS_2 islands grown from the procedure shown in the top of Figure 3b of trilayer synthesis. (a) Optical photograph of MoS_2 crystals on Si/SiO_2 containing monolayer (1L), bilayer (2L) and trilayer (3L) crystals. (b) Raman intensity map of the area shown in the red rectangle in (a) recorded at 383 cm^{-1}. (c) Raman spectra of monolayer (1L) and bilayer (2L) MoS_2 triangles from (b). (d) AFM image of the area shown in the green rectangle in (a). (e) Height profiles measured along the dashed lines in (d)...17

Figure 5 AFM images of uniform monolayer (a), bilayer (b) and trilayer (c) MoS_2 crystals. (d) Height profiles measured along the dashed lines in (a-c). 19

Figure 6 Comparison of optical (a) and PL (b) images of MoS_2 crystals.........................20

Figure 7 (a-c) CVD grown MoS_2 triangles on Si/SiO_2 recorded by (a) SEM (5 kV), (b) SEM (1 kV), (c) optical microscopy. (d-f) Exfoliated MoS_2 flakes on Si/SiO_2 recorded by (d) SEM (5 kV), (e) SEM (1 kV), (f) optical microscopy. (g) Raman spectra recorded from the spots shown in panels (c) and (f) for different thicknesses of MoS_2 crystals. 22

Figure 8 Electrical measurements of CVD-grown MoS_2 crystals. (a) Transfer characteristics of the MoS_2 device show in the inset. (b) Semi-logarithmic scale of the I_{sd}-V_g from panel (a) with an inset of the I_{ds}-V_{ds} at different gate voltages (ranges -40 to 40 V with a 20 V step). (c) Optical photographs of a monolayer (1L), bilayer (2L) and trilayer (3L) MoS_2 triangle device. (d) Transfer characteristics of devices 1L, 2L and 3L MoS_2 devices from (c). 24

Figure 9 Differing shapes of WS_2 islands in the form of triangles (left), stars (middle) and merging islands (right). 30

Figure 10 Raman map collected at 521 cm^{-1} of the area enclosed in a red rectangle shown in the inset. 31

Figure 11 Multiple nucleation sites on the surface of a WS_2 crystal. 33

Figure 12 Raman spectra of monolayer (1L), bilayer (2L) and multilayer (ML) WS_2 crystals shown in the inset. 35

Figure 13 AFM showing the height of a thick multilayer WS_2 crystal closest to the sulfur source. Change in vertical height (Δh). 36

Figure 14 Optical image of single layer WS_2 device (left). Mobility of WS_2 device (right) with an inset showing I_{DS}-V_{SD} dependencies measured at different gate voltages from -40 V to 40 V with a 20 V step. 38

Figure 15 Few-layer graphene on boron nitride. 45

Figure 16 Single layer graphene devices with transfer characteristics and mobilities from -40 V to 40 V. (a and c) Graphene on boron nitride and (e) graphene on SiO_2. (b) Transfer characteristics of (a) showing a Dirac point around -3 V. (d) Transfer

characteristics of (b) showing a Dirac point around 3V. (f) Transfer characteristics of (e) showing a Dirac point outside of the measured range. 46

Figure 17 Few-layer graphene device on boron nitride. (a) Optical image. (b) Transfer characteristics of MoS_2 device shown in (a). (c) I_{SD}-V_{SD} dependencies measured at different gate voltages ranging from -40 V to 40 V with a 10 V step. (d) Mobility calculation based on the transfer characteristics shown above. 48

Figure 18 (a) Few-layer graphene on both boron nitride and PZT. (b) Enlarged area of (a) showing the difference between the graphene on boron nitride/PZT (left portion) and just PZT (right portion). Device fabricated of the graphene on (c) boron nitride/PZT. and (d) PZT. 50

Figure 19 Transfer characteristics of Gr-PZT (left) and Gr-BN-PZT (right), where Gr stands for graphene and BN stands for boron nitride. 51

Figure 20 A second layer of boron nitride placed on top of the graphene previously laid upon a boron nitride flake with a top-gate FET (top). Transfer characteristics of the device shown above at different voltages ranging from -1 V to 1 V through -5 V to 5 V (bottom)..53

Figure 21 Optical image demonstrating MoS_2 nucleation being favored at the edges of boron nitride (left). SEM image of the optical image from the left panel of MoS_2 growth around and on top of boron nitride (right). 58

Figure 22 SEM image demonstrating the alignment of MoS_2 triangles compared to the edges of boron nitride. 60

Figure 23 Optical image of very thin boron nitride flake containing multiple thicknesses of few layers prior to MoS_2 growth (left). SEM image of MoS_2 grown on/around the

boron nitride flake with no epitaxial alignment or very little triangular growth seen (right). 61

Figure 24 SEM image of boron nitride with thickness ranging from double layer (red) to greater than 100 layers (green), the thinnest parts showing no epitaxy and the thicker areas with good alignment can be seen in Figure 22. 62

Figure 25 AFM confirming single layer MoS_2 triangles are grown in the thicker region of boron nitride. Change in vertical height (Δh). 63

Figure 26 Raman of the optical image from the inset. The black dot corresponds to the Raman shown in black confirming growth of WS_2.The red dot corresponds to the Raman shown in red confirming growth of MoS_2. 68

Figure 27 Optical image of a heterostrucutre (left). Raman maps taken of the sample from the left panel. Raman map of MoS_2 recorded at 403 cm^{-1} (middle) and Raman map of WS_2 recorded at 351 cm^{-1} (right). 69

Figure 28 AFM from the center region to the outer region similar to the flake shown in Figure 25 showing no discernable change in the height between the two structures. 70

Figure 29 PL map of the same sample shown in Figure 27. 72

Figure 30 Primary attempt at measuring electronic properties of an in-plane MoS_2/WS_2 heterostructure device. 73

CHAPTER 1: MOLYBDENUM DISULFIDE

Background

The discovery of graphene, a sp^2 hybridized planar sheet of carbon atoms, has caused an eruption of new two dimensional materials to be studied. Graphene's unique properties, such as its strength,[1] flexibility,[1,2] high charge carrier mobility,[3–5] high surface-to-volume ratio[6] and transparency,[7,8] are different from the properties of its bulk counterpart, *i.e*. graphite, and highly desired for a number of applications, including RF transistors, gas sensors and transparent conductors among others.

The major problem with graphene for electronic applications is its lack of an energy band gap. Band gap refers to the energy required to excite an electron from the valence band to the conduction band so that it may conduct electricity. Graphene's band structure is unique because it consists of two cones touching at the tips, or Dirac points.[9] In these cones, the two-dimensional energy dispersion relation is linear making electrons and holes degenerate.[10,11] Since graphene does not have a band gap, it acts like a semimetal, giving it a very poor on/off ratio in field-effect transistors (FETs) of up to ~5^5. Its shortcomings are what have led to the interest in alternative two-dimensional materials with semiconductor properties.

Other materials in the graphene family include hexagonal boron nitride (often referred to as "white graphene"),[12] boron carbon nitride (BCN),[13] fluorographene[14] and graphene oxide[7] among others. "White graphene" is an insulating material, so it cannot be used as a device channel, although it finds applications as a substrate dielectric for

improved graphene based devices.[12] The other materials, such as fluorographene, mentioned to be in the same family of graphene have proven thus far to have very poor electronic qualities[14] or are non-stoichiometric making them difficult to control.[15,16] A second set of materials that exist as two-dimensional materials are oxides, which are more stable in air than many monolayer materials, but also more susceptible to changes when in contact with water and protic solvents. This poses many problems for the entire family of oxides outside of simply stability, their use in reactions would be limited as well as characterization and fabrication techniques diminished.[17]

A very most promising group of two-dimensional materials, most of which actually have semiconductor properties, are transition metal dichalcogenides (TMDs), of which the most prominently studied two-dimensional material up to this point besides graphene has been molybdenum disulfide (MoS_2).[17–21] TMDs have a transition metal (e.g., Mo, W, Nb, Ta) "sandwiched" between two chalcogen layers (e.g., S, Se, Te). Graphene and TMDs share many similarities characterized by noncovalent bonding between layers and strong in-plane covalent bonding.[17]

Majority of studies use MoX_2 and WX_2 because they have been shown to be semiconducting, whereas NbX_2 and TaX_2 are metallic making them less versatile for transistor applications.[22–25] Regardless of bulk or monolayer, the band gaps of many TMDs are comparable to or exceed that of the 1.1 eV of silicon.[26] One of the most important properties of MoS_2 is that as a crystal it has an indirect band gap of ~1.3 eV, and as the number of layers decreases to a monolayer, it becomes a semiconductor with a direct band gap of ~1.9 eV.[27] The reason for an increase in the band gap is generally due to confinement of carriers in the out-of-plane direction inducing a gradual increase in the

band gap with decreasing thickness.[28] Since the monolayer MoS_2 has a direct band gap, it is promising for the electronics industry, which is driven by scaling down the size of transistors and is reaching the limit for current silicon-based transistors.[26]

Current field-effect transistors (FETs) use a semiconducting channel region connected to source and drain electrodes that are made of an inert conducting material, *i.e*. gold, while an insulating layer, such as silicon oxide (SiO_2), is used as a gate dielectric.[29] The current that flows between the source and drain electrodes through the semiconducting channel can be modulated by the voltage applied to the gate electrode. There are many different factors that can affect the electronic characteristics of a device, specifically the mobility of carriers is affected by different types of scattering, such as Coulombic impurities,[30] surface interfacial phonons and roughness scattering.[4,12,31] Minimizing these scattering effects can lead to improved mobilities in FETs and bring the characteristics of current devices closer to theoretical calculations. This study includes results of FET measurements of TMD materials, as well as describes efforts on minimization of scattering effects in TMDs by growing them on atomically flat crystalline hexagonal boron nitride substrates.

Introduction

As the most studied TMDs, MoS_2 has been found to have a large number of applications such as its use in field-effect transistors (FETs) due to its high on-off ratios,[32–34] gas sensors with its n-type semiconducting nature,[35] photodetectors,[36] optoelectronics such as ferroelectric memories,[37] and energy storage in batteries.[38] The reason MoS_2 has been favored over materials utilizing tungsten or selenium is because of the larger availability of molybdenite crystals, and their higher chemical stability

compared to most other TMDs. After becoming "the standard" for TMD, MoS_2 growth has been studied in a multitude of ways.

Because of the weaker out-of-plane bonding, it very easy to mechanically exfoliate single to few layers of these materials from the bulk crystals. Mechanical exfoliation is simply the peeling away of a material layer by layer, which in the case of graphene and TMDs is the disruption of weak van der Waals attractions. The most common way to exfoliate these materials is using adhesive tape to overcome the van der Waals forces holding the layers together.[39] This top-down approach of preparing these single to few layered materials has many problems which are difficult to overcome, such as reproducibility, uniformity and the size of the flakes created. Alternative exfoliation techniques of TMDs and other two-dimensional materials are not limited to the mechanical exfoliation, liquid-phase exfoliations have also been performed.[40] In one method, it was found that the flakes exfoliated in this manner were monolayer with sizes of <1 μm, and since lithium is used, it increases the cost and risk of flammability. A second liquid-phase technique, involves the use of sonication in different solvents such as isopropanol, dimethylformamide, dimethyl sulfoxide, and cyclohexanone.[41] and surfactant solutions, *e.g.* sodium cholate, taurodeoxycholate, lithium dodecyl sulfate, and others.[42] These methods are much safer and cost effective than using lithium intercalation but give low yield of monolayer flakes.

Despite the problems, mechanical exfoliation of graphene using tape has shown the best results in terms of physical and electrical properties.[4] Likewise, much research has been done on exfoliated flakes of MoS_2, but a different approach to making these materials is bottom-up synthesis where the materials are synthesized at the atomic level.

Chemical vapor deposition (CVD) has allowed for the synthesis of large-scale, large-area growth of single layer MoS_2 not reproducible via exfoliation, although the CVD-grown MoS_2 is still routinely compared to the top-down exfoliated samples.[34] The most common CVD techniques of producing MoS_2 rely on sulfur powder and a separate source of molybdenum, such as MoO_3,[43–48] $MoCl_5$,[49] or metallic molybdenum.[50] Other CVD techniques that have been done are the vapor phase transport and recrystallization of MoS_2,[51] thermal decomposition of $(NH_4)_2MoS_4$,[52] and metal-organic CVD.[53]

The growth of MoS_2 is predominately triangular with a single nucleation point leading to monolayer islands that grow outward, potentially merging with nearby islands to form lager continuous monolayers. Although the grain boundaries between domains of merging islands do not affect the electronic properties as seen in the individual triangles of MoS_2,[47] they are still most often used in research because their shape can be correlated with the MoS_2 crystallographic orientations. There have been other growth types reported, *i.e*. star shaped[54] and hexagonal,[48,55] that form due to differences in procedure that lead to alteration of growth kinetics or the amount of chalcogen used.

While most studies pertain to the monolayer MoS_2, very little work has been done on multilayer MoS_2, especially uniform bilayer and trilayer MoS_2 triangular islands. Some unique properties that multilayer two-dimensional materials possess over their monolayer counterparts originate from different van der Waals interactions between the layers. The different ways the layers of MoS_2 can grow on top of one another has been studied extensively to differentiate between stacking order; a 0° twist angle between two layers (AB stacking) and a 60° twist angle (AA' stacking) being the major conformations.[56] The stacking configuration can play an important role in the size of the

band gap, changing with the twist angle[57]. The van der Waals interactions between layers are what eliminate the direct band gap of MoS_2 and create an indirect one, which explains the absence of photoluminescence in few-layer MoS_2 compared to monolayer crystals.[21]

In this chapter, a CVD procedure is established that yields continuous bilayer and trilayer MoS_2 islands. Characterization via Raman spectroscopy, atomic force microscopy (AFM) and photoluminescence (PL) microscopy provides data that conforms to what has already been established for single to multilayer MoS_2. Due to the difference in the band gap type (direct *versus* indirect) as seen by the stark contrast in PL, it was determined that monolayers of MoS_2 could also be differentiated from few-layers with scanning electron microscopy (SEM) at very low accelerating voltages. After confirming the results, electrical measurements were also performed on monolayer and few-layer MoS_2 flakes.

Experimental Procedure

MoS_2 crystals were grown on p-doped silicon substrates covered with 300 nm-thick silicon oxide (SiO_2). Substrates were cleaned for 10 minutes in acetone, 10 minutes in deionized water, and 10 minutes in 2-propanol before being put into a UV ozone cleaner, ProCleaner™ Plus system for 30 minutes. Once the substrates are clean, 0.5-1 mg of molybdenum (VI) oxide (99.95%, Alfa Aesar) was placed into the center of a clean 40 mm quartz boat. One substrate (1 x 0.25 cm^2) was placed with the SiO_2 layer facing away from the MoO_3 (indicated face-up) directly over the center of the MoO_3 and the second substrate (~2 x 2 cm^2) was placed with the SiO_2 layer facing toward the MoO_3 (face-down) with one edge aligned over center of the MoO_3. The quartz boat was then loaded into a 2-inch quartz tube in a Lindberg Blue M tube furnace. A second quartz boat

was prepared with 50 mg of sulfur (99.999%, Acros Organics) and placed ~35 cm upstream of the MoO_3, over the center of a hotplate. The CVD setup can be seen in Figure 1a.

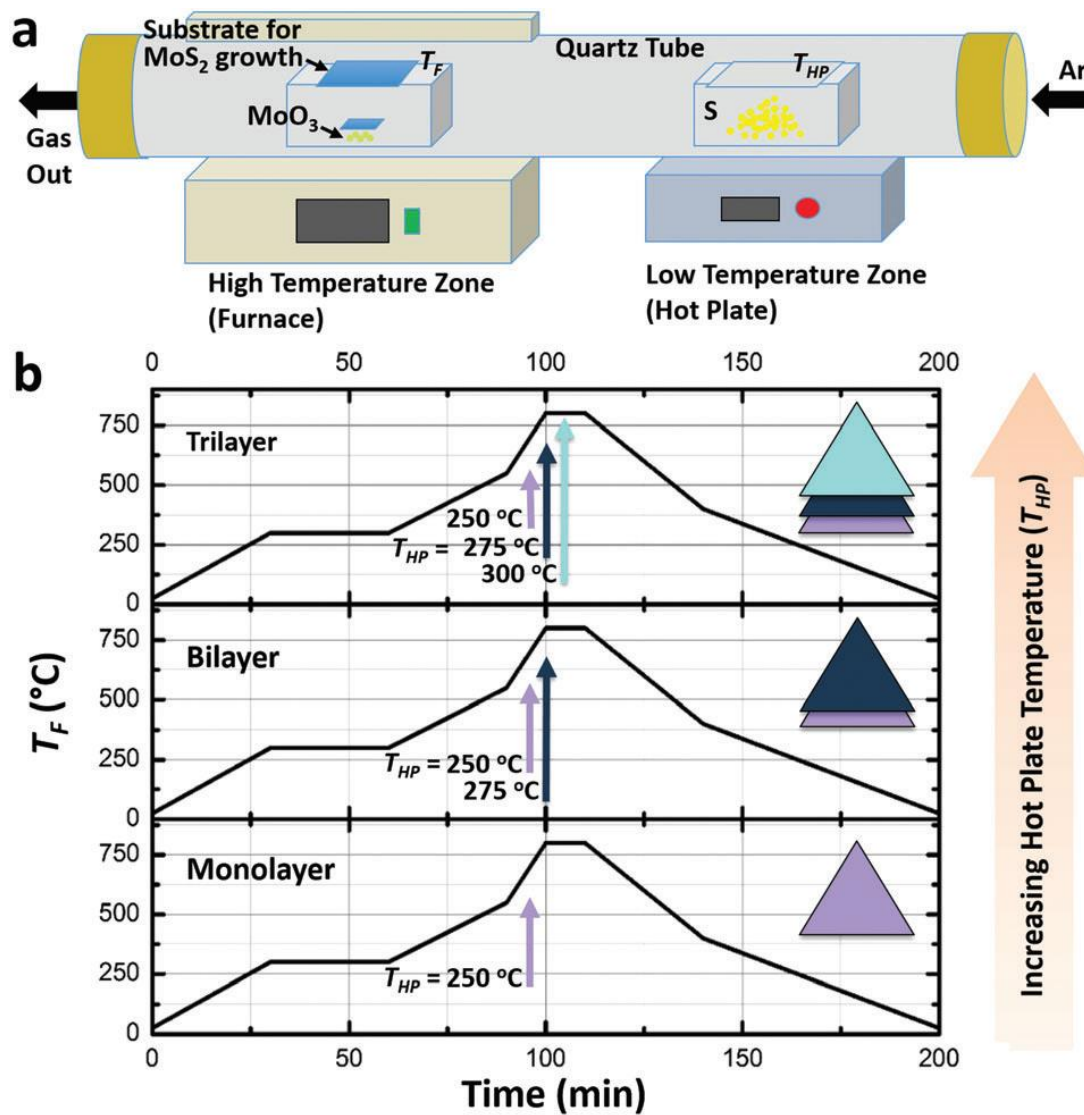

Figure 1 CVD growth of MoS_2 islands with different thicknesses. (a) Scheme of the CVD setup. (b) Experimental parameters for growing MoS_2 with a different number of layers. T_F represents the temperature of the furnace and T_{HP} represents the temperature of the hotplate. Arrows indicate the time when T_{HP} is increased and held constant.

The system was flushed with argon three times and the growth procedure was performed at atmospheric pressure with 100 sccm of argon flowing throughout the growth procedure. The CVD procedure starts as the temperature goes up to 300 ºC over 30 minutes, remains at 300 ºC for 30 minutes, then climbs to 550 ºC over 30 minutes to remove any water or surface contaminates that remained after cleaning. After reaching 550 ºC the temperature is further increased to 800 ºC over 10 minutes, held at 800 ºC for 10 minutes, and cooled slowly until 380 ºC before opening the furnace to cool back to room temperature.

To produce single layer MoS_2 the above procedure was followed by increasing the temperature of the hot plate, T_{HP}, to 250 ºC at 5 minutes before the temperature of the furnace, T_F, reaches 800 ºC. Monolayer MoS_2 triangles were grown similarly to previously reported studies.[58] In order to produce multilayer MoS_2 the same procedure as above was followed except with a change to the rate of sulfur evaporation. By increasing the T_{HP} to 275 ºC when T_F reaches 800 ºC a bilayer of MoS_2 was produced. If T_{HP} is increased again to 300 ºC after 5 minutes at 800 ºC, an allotment of trilayer MoS_2 islands form.

Raman spectroscopy was performed using a Thermo Scientific DXR Raman microscope with a 532 nm laser. SEM images were taken using a Hitachi S4700 field emission scanning electron microscope in secondary electron detection mode at the accelerating voltage of 5 kV. Atomic force microscopy (AFM) images were recorded using a Bruker Dimension Icon Atomic Force Microscope equipped with ScanAsyst. Photoluminescence (PL) microscopy was performed using a Nikon Eclipse Ti-E inverted

microscope with a Cy5 filter cube with an excitation cut-off at ~652 nm and an emission cut-off at ~671 nm.

For device fabrication, a Zeiss Supra 40 field-emission scanning electron microscope and a Raith pattern generator were used for electron beam lithography (EBL) and an AJA electron beam evaporator was used for electron beam evaporation (EBE), the detailed procedure for the device fabrication can be found elsewhere.[59] Electrical measurements of the devices mentioned above were performed using a Lake Shore TTPX cryogenic probe station at a base pressure of ~2 x 10^{-6} Torr. The device electrodes were connected to an Agilent 4155C semiconductor parameter analyzer that was linked to a computer through 82357B USB/GPIB interface and controlled using a National Instruments LabView code.

Results and Discussion

Earlier work done in this field had yielded a method of getting single layer flakes of MoS_2 but not quite as consistently in shape or quality as was desired. The process of growing consistent single layer MoS_2 triangular islands was adapted from previous work by tweaking growth points and additional parameters, see Experimental section for optimized growth conditions currently used. By adjusting the conditions, more uniform triangular islands of MoS_2 could be seen all around the substrate rather than a mix of triangles, stars, hexagons, and merging islands, Figure 2.

Star-shaped MoS_2 tends to occur when the cooling time was fast, not allowing the sulfur enough time to reach the MoO_3 and to fully react. More complete triangular islands were grown by turning the hotplate on earlier in the process rather than after maximum temperature was reached or once cooling began rather than the star shapes originally

seen. Formation of hexagons and merging islands of MoS_2 was reduced by limiting the amount of MoO_3 allowed to reach the second/larger substrate. To limit the overall nucleation that can occur and restrict the number of merging islands, the amount of MoO_3 used was reduced and a smaller substrate was placed between the desired substrate and molybdenum source.

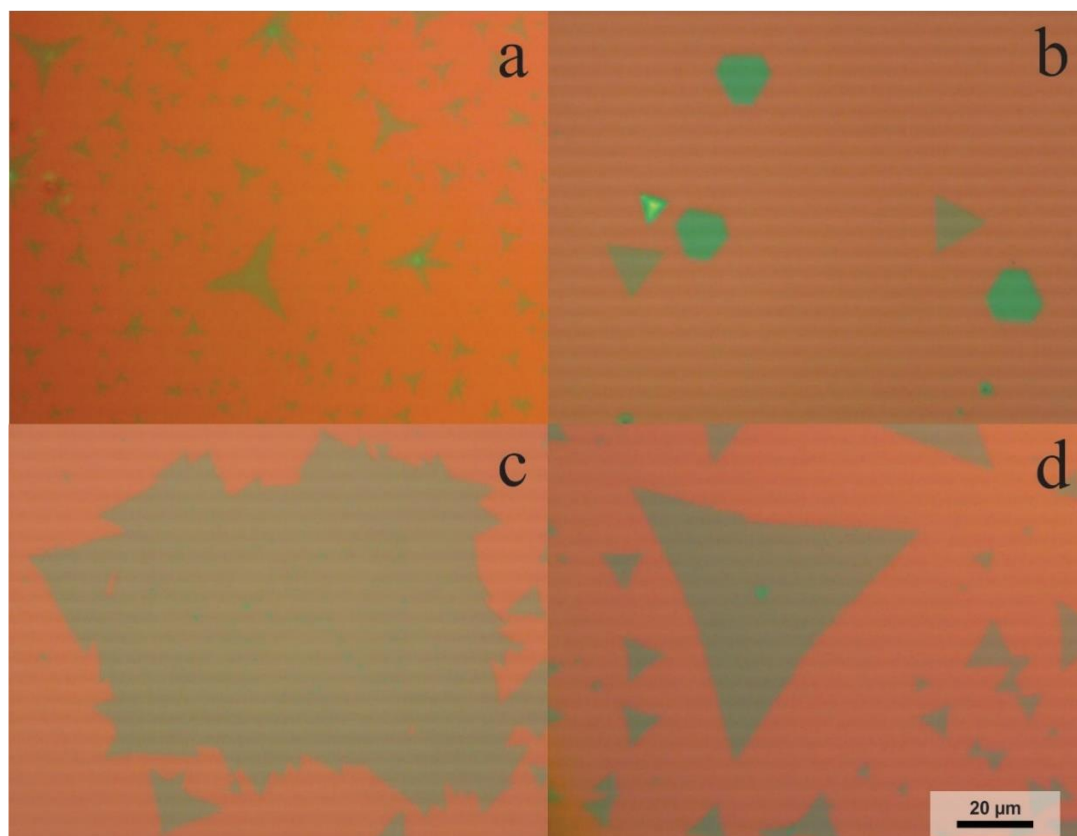

Figure 2 Different shapes of MoS_2 islands in the form of stars (a), hexagons (b), merging islands (c) and uniform triangles (d). Scale bar is the same for all images.

After consistent growth of uniform MoS_2 triangular islands the next task was to try and grow uniform layered triangles. As could sometimes be seen in the adjusted growth procedure, some of the triangles formed had a very clear nucleation site visible in the center of the triangle and even some with growth occurring off that nucleation site presenting the beginning of a second layer Figure 2d. The assembly of a second layer on top of a single layer is something that has already been studied in detail but almost no work has been done on a uniform few layer islands of MoS_2.

The areas that seemed to have more appearances of a bilayer on the substrate were closer to the center of the boat where the oxide is originally placed, indicating that the area nearer the sulfur may grow taller structures. A possible explanation for these thicker islands was due to a faster rate of sulfurization. Unfortunately, it was not the case for when the rate of sulfur was simply increased by raising the temperature of the hotplate immediately upon reaching growth temperatures, no thicker uniform islands were seen. An array of different temperatures was tested, every 5 ℃ upward of 250 ℃ all the way to 300 ℃, but nothing different grew than at the initial 250 ℃ introduction point. In fact, even fewer structures were seen overall than before and even less uniform in shape than the previously shown. This was most likely due to the sulfur simply flowing past the molybdenum faster than it was depositing on the substrate creating less opportunity for growth to occur.

As a result of less growth with an increase in temperature, the idea that the monolayer triangles needed time to properly form before the second layer formation can begin emerged. To allow time for a monolayer to grow, the procedure for single layer triangular islands was used and after 5 minutes, the temperature of the hot plate was

increased in three separate experiments first by 10 ºC, then 20 ºC and 30 ºC, respectively, to see if growth of a second layer would form if the nucleation site atop the monolayer was given time to form first. Incomplete growth was seen at 260 ºC leaving more monolayer islands at the early stages of the second layer formation. More uniform bilayer triangles were then seen at the 20 ºC and 30 ºC increases but at 280 ºC the triangles appeared to be smaller than the complete bilayer found at 270 ºC. It was decided that the rate of sulfur deposition was too fast, and the second layer was reaching the edge of the still growing single layer inhibiting the growth. Without enough energy in the system, the second layer of MoS_2 will halt the first layer from continuing to expand outward because the second layer will grow at a faster rate than the first due to more sulfur being deposited faster at the nucleation site. As such, the sulfur flow rate at 280 ºC was limiting the growth of the triangles, and 275 ºC was used to encompass both better size and uniformity.

At the creation of a uniform bilayer MoS_2 triangle, the idea to expand this to a third layer by the same process was decided. After allowing time for the bilayer to begin forming, the temperature was increased again by 25 ºC. A sample produced by this final approach is shown in Figure 3 with labelled monolayer, bilayer and trilayer MoS_2 crystals (the same area of the same without labels is shown in Figure 4a). It is easy to distinguish monolayer MoS_2 just by the optical contrast on 300 nm-thick SiO_2 under an optical microscope, while the bilayer and trilayer islands can be differentiated by color. The thickness of the crystals was also verified by Raman spectroscopy, AFM and PL microscopy. All of the MoS_2 crystals in Figure 3 are labelled to indicate the number of layers; of the 123 islands shown. Only 19 are monolayer (15.5%), 72 are bilayer (58.5%)

and 32 are trilayer (26%). For the growth procedure of trilayer MoS_2 as depicted in Figure 1, the sample shows an area of 84.5% multilayer growth but with other areas of varied growth scattered throughout the substrate, but several comparable areas were commonly seen. This makes for very simple identification of large (>10 μm) uniform bilayer and trilayer MoS_2 crystals.

Characterization of these flakes was done with several different techniques. Raman spectroscopy can differentiate between monolayer, bilayer and trilayer MoS_2 crystals based on spectral positions of the E_{2g}^1 (~383 cm^{-1}) and A_{1g} (~405 cm^{-1}) modes.[60,61] As the number of layers in a MoS_2 crystal increases, the separation between the E_{2g}^1 peak and A_{1g} peak grows from ~19 cm^{-1} (monolayer) to ~25 cm^{-1} (bulk)[60]. Figure 4b shows a Raman intensity map of the area outlined by the red square in Figure 4a at 382 cm^{-1} demonstrating that bilayer MoS_2 crystals give a higher Raman intensity than that of monolayer crystals. Figure 4c shows a representative Raman spectra recorded for both the monolayer and bilayer MoS_2 triangles shown above.

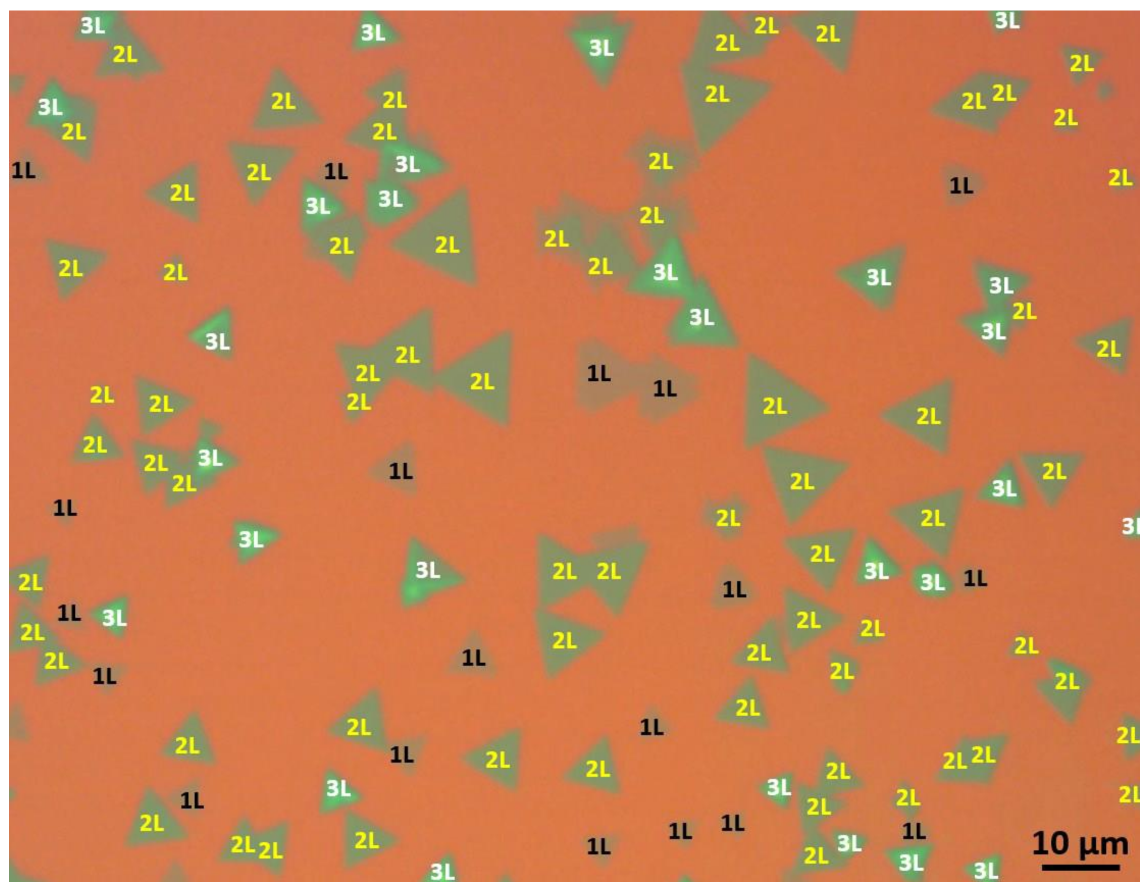

Figure 3 Optical photograph of a Si/SiO_2 substrate with monolayer (1L), bilayer (2L) and trilayer (3L) MoS_2 islands with single nucleation sites.

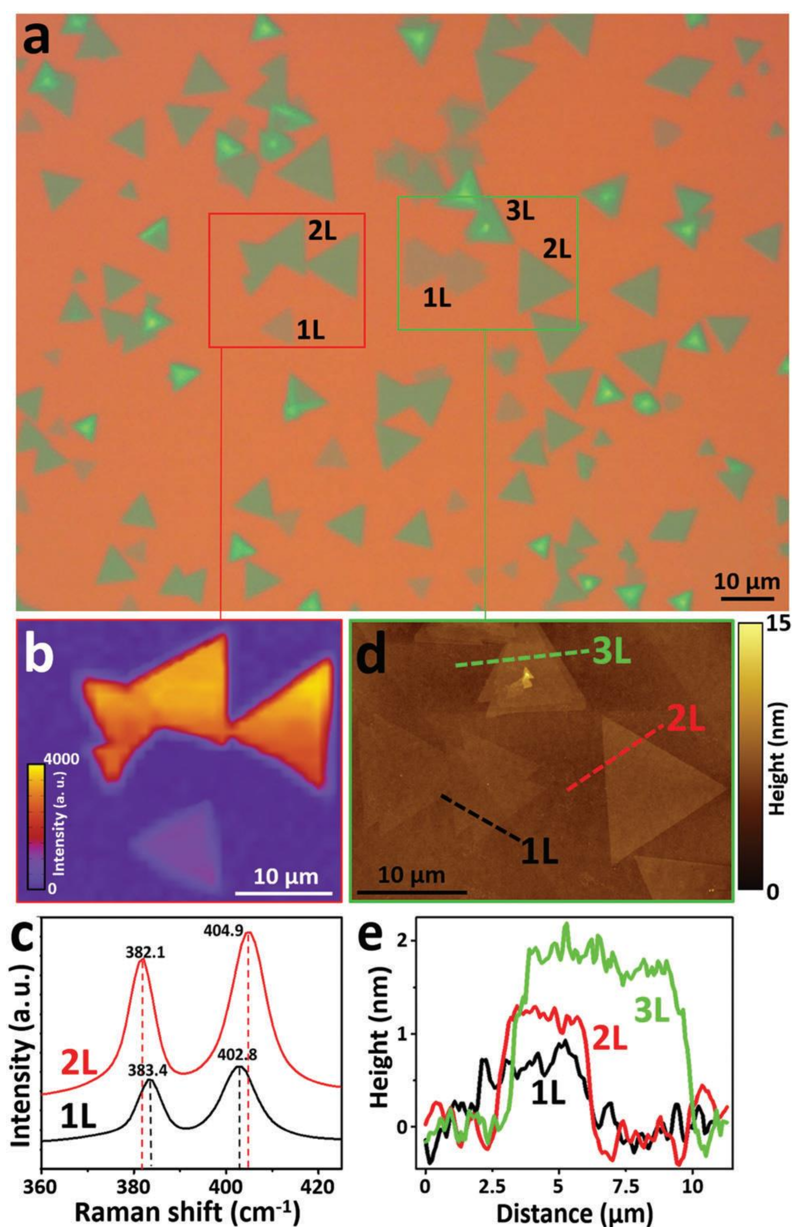

Figure 4 Characterization of MoS_2 islands grown from the procedure shown in the top of Figure 3b of trilayer synthesis. (a) Optical photograph of MoS_2 crystals on Si/SiO_2 containing monolayer (1L), bilayer (2L) and trilayer (3L) crystals. (b) Raman intensity map of the area shown in the red rectangle in (a) recorded at 383 cm^{-1}. (c) Raman spectra of monolayer (1L) and bilayer (2L) MoS_2 triangles from (b). (d) AFM image of the area shown in the green rectangle in (a). (e) Height profiles measured along the dashed lines in (d).

Another technique used to measure thickness of MoS_2 crystals is AFM. The AFM shown in Figure 4d is of the area outlined by the green square in Figure 4a. According to the height profiles given by the dashed lines intersecting the triangles shown in Figure 4d the area contains monolayer (1L), bilayer (2L) and trilayer (3L) MoS_2 crystals. The monolayer measured in Figure 4e gives a thickness of ~0.7 nm which is consistent with previously reported literature of other CVD-grown MoS_2 triangles[44]. If the heights add up as expected, then it follows that the bilayer should have a thickness of ~1.3 and trilayer a thickness of ~2.0, which in fact they do. While the trilayer in this sample is actually terraced, not uniform, it gave a good representation of how all three layers can grow in the same area. A uniform trilayer crystal that could be observed in many places on the flake is show in Figure 5c. Figure 5a-c shows how similar the three different layers of MoS_2 triangles may appear, only differing in height (Figure 5d).

Since bulk MoS_2 all the way down to bilayer has an indirect band gap while monolayer has a direct band gap, the difference between monolayer and multilayer can be distinguished by PL microscopy. Figure 6 shows images of optical and PL microscopy of a sample grown with bilayer conditions previously mentioned with a maximum T_{HP} of 275 ºC. Although monolayer MoS_2 crystals show a bright emission in Figure 6b, multilayer crystals remain dark, except for the edges. The reason some of the monolayer crystals do not look as uniform has been reported to be the result of sulfur deficiency.[43] PL shows a more detailed image of monolayer MoS_2 flakes. However, PL is impractical on samples with flakes thicker than one layer, or to differentiate between thicknesses beyond one to two layers.

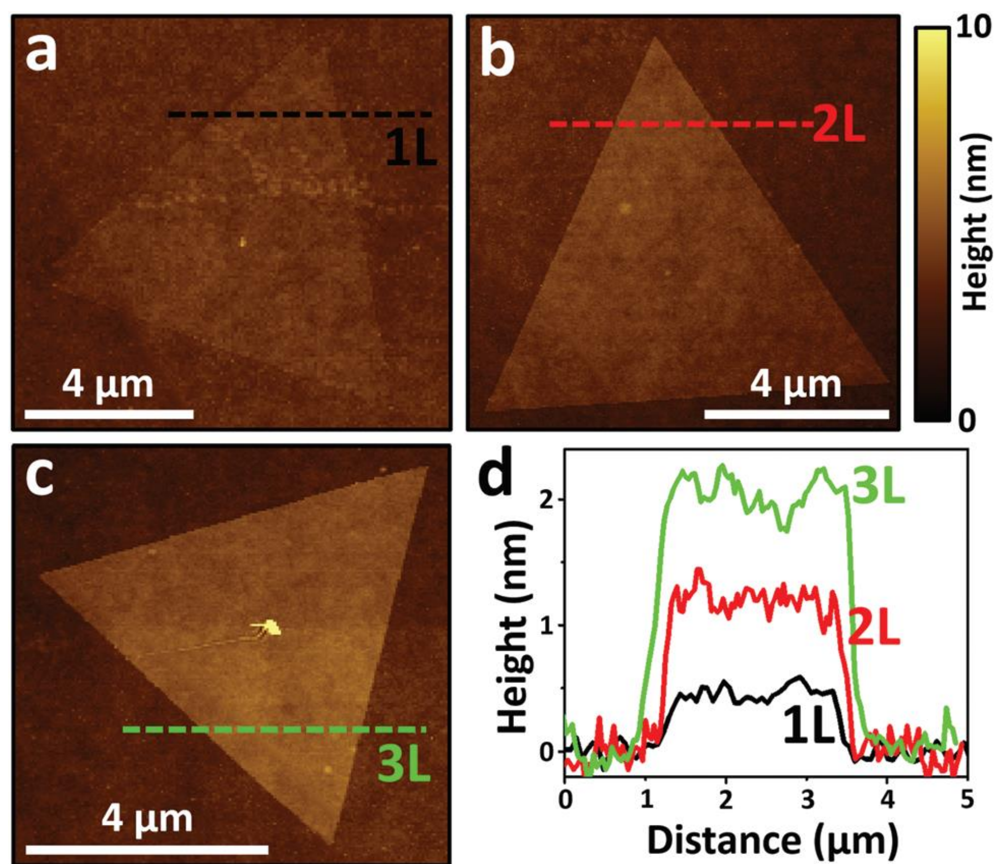

Figure 5 AFM images of uniform monolayer (a), bilayer (b) and trilayer (c) MoS_2 crystals. (d) Height profiles measured along the dashed lines in (a-c).

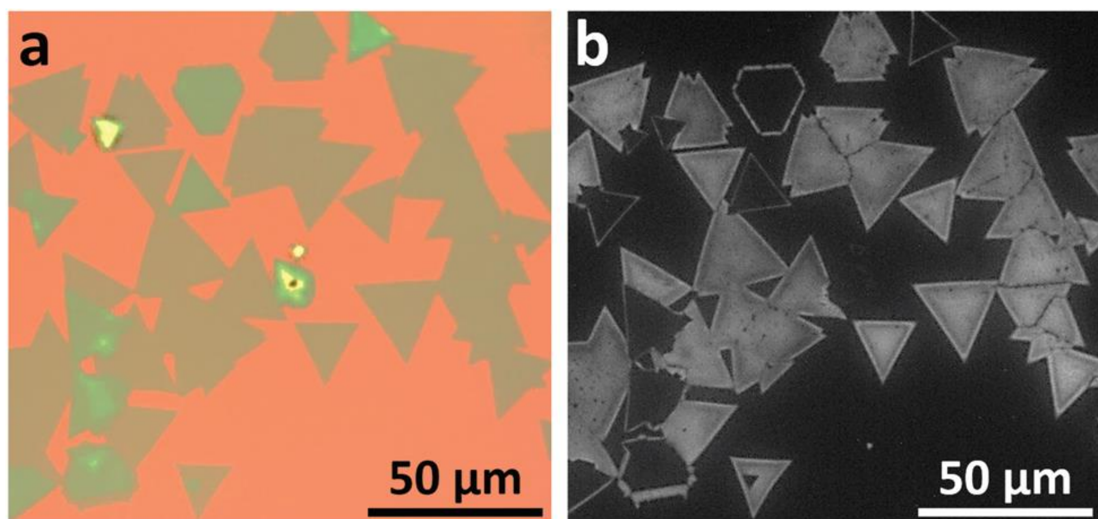

Figure 6 Comparison of optical (a) and PL (b) images of MoS_2 crystals.

To reinforce what has been demonstrated on the growth and characterization of CVD grown MoS_2 it was compared to mechanically exfoliated MoS_2 flakes from a single crystal (SPI Supplies) via adhesive tape and transferred to a Si substrate with a 300-nm-thick SiO_2 layer for similar comparison as seen in Figure 7d-f. The exfoliated area shown in Figure 7f contains monolayer (1L), bilayer (2L), trilayer (3L), and bulk MoS_2 crystals. The CVD-grown MoS_2 and exfoliated MoS_2 were verified with Raman spectroscopy, see Figure 7g. In both cases, the 1L and 2L regions are indistinguishable by their brightness in SEM at 5 kV (Figure 7a and 7d). However, at 1 kV, the monolayer regions of MoS_2 crystals appear much darker than the bilayer regions seen in Figures 7b and 7e. This demonstrates a new and useful way to quickly screen for monolayer MoS_2 similarly seen in PL spectroscopy.

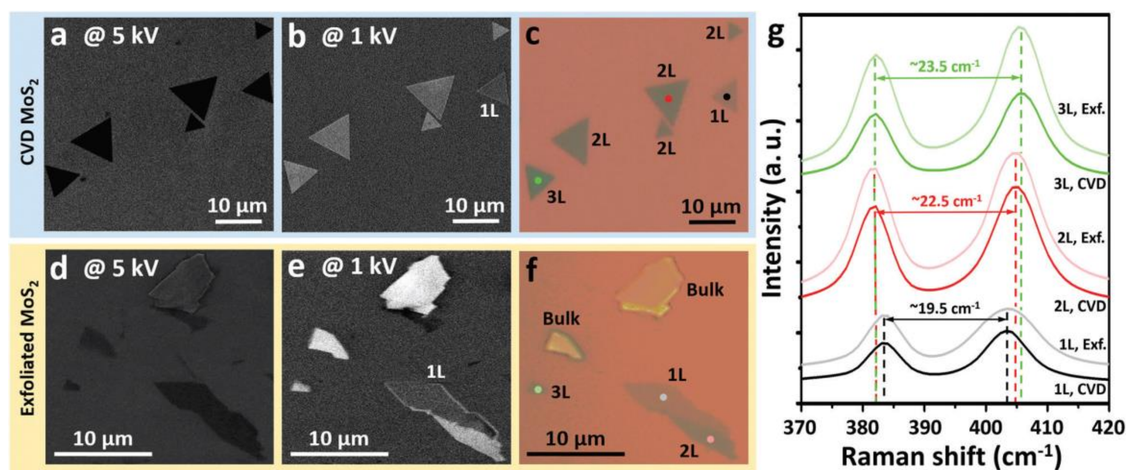

Figure 7 (a-c) CVD grown MoS_2 triangles on Si/SiO_2 recorded by (a) SEM (5 kV), (b) SEM (1 kV), (c) optical microscopy. (d-f) Exfoliated MoS_2 flakes on Si/SiO_2 recorded by (d) SEM (5 kV), (e) SEM (1 kV), (f) optical microscopy. (g) Raman spectra recorded from the spots shown in panels (c) and (f) for different thicknesses of MoS_2 crystals.

Finally, the electronic properties of the CVD-grown MoS_2 crystals on Si/SiO_2 substrates were assessed. Ti/Au (1 nm/20 nm) electrodes were fabricated onto MoS_2 crystals. A FET shown in Figure 8a depicts a MoS_2 channel bridging two Ti/Au source (S) and drain (D) electrodes on Si/SiO_2. The silicon was used as a back gate (G) and is heavily doped toward the p-type silicon. The devices were allowed two days of evacuation in order to minimize the effect of surface adsorbates[62].

Figure 8a demonstrates the properties of a monolayer MoS_2 FET with a n-type source-drain current (I_{SD})-gate voltage (V_G) dependence with electron mobilities reaching 2.5 $cm^2\ V^{-1}\ s^{-1}$. The source-drain current (I_{SD})-source-drain voltage (V_{SD}) dependences are Ohmic at all gate voltages (Figure 8b insert). A semi-logarithmic scale of the same n-type I_{SD}-V_G dependence shows the device has an ON/OFF ratio of ~10^5, Figure 8b. In total, 15 devices based on monolayer MoS_2 triangles were measured and show consistent electron mobilities of $2.7 \pm 0.9\ cm^2\ V^{-1}\ s^{-1}$ with ON/OFF ratios ranging from 10^3 to 10^5. Devices made of bilayer and trilayer MoS_2 crystals exhibited similar properties.

A comparison of the conductivity between the different layers of devices optically shown in Figure 8c can be seen below in Figure 8d. From the graph, it can be seen, that as the number of layers increases so does the conductivity. The electron mobilities reach 3.1 $cm^2\ V^{-1}\ s^{-1}$ for 1L MoS_2, 4.5 $cm^2\ V^{-1}\ s^{-1}$ for 2L and 9.5 $cm^2\ V^{-1}\ s^{-1}$ for 3L. Overall, eight bilayer MoS_2 FETs were measured with an average mobility of $4.7 \pm 1.6\ cm^2\ V^{-1}\ s^{-1}$ and seven trilayer MoS_2 FETs with an average mobility of $7.3 \pm 2.3\ cm^2\ V^{-1}\ s^{-1}$. The ON/OFF ratios for each multilayer measured had the same range as monolayer, 10^3 to 10^5.

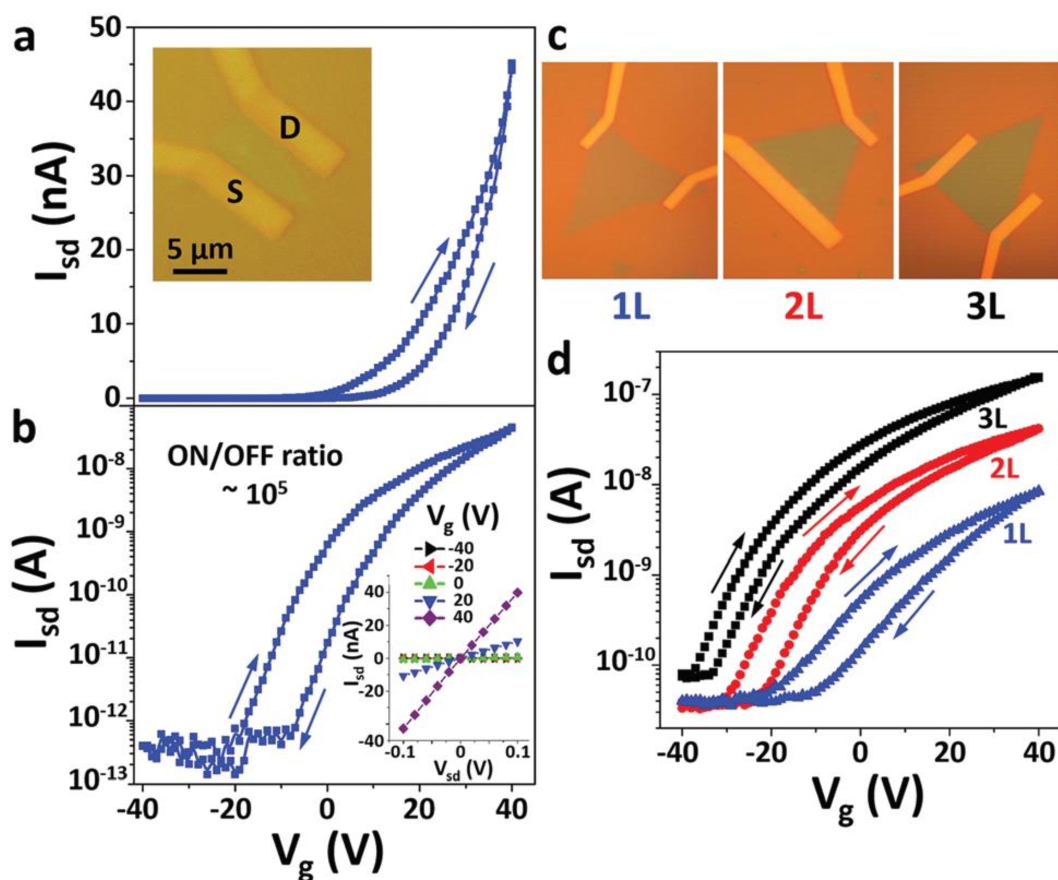

Figure 8 Electrical measurements of CVD-grown MoS_2 crystals. (a) Transfer characteristics of the MoS_2 device show in the inset. (b) Semi-logarithmic scale of the I_{sd}-V_g from panel (a) with an inset of the I_{ds}-V_{ds} at different gate voltages (ranges -40 to 40 V with a 20 V step). (c) Optical photographs of a monolayer (1L), bilayer (2L) and trilayer (3L) MoS_2 triangle device. (d) Transfer characteristics of devices 1L, 2L and 3L MoS_2 devices from (c).

In summary, the new growth procedure for MoS_2 crystals grown in CVD from MoO_3 and sulfur yield prominently bilayer and trilayer MoS_2 islands. Additional layers can only form after the initial nucleation and growth of the monolayer has occurred. This method allows for uniform bilayer and trilayer islands rather than the more often reported terraced structures,[56,57] although some terraced growth does still occur. It was revealed that along with traditional forms of characterization for MoS_2 (Raman spectroscopy, AFM and PL microscopy), SEM can also be used to distinguish between monolayer and few-layered MoS_2 flakes at low accelerating voltages. Lastly it was demonstrated that electron mobility increases with increasing layer counts.

CHPATER 2: TUNGSTEN DISULFIDE

Introduction

Another well-studied TMD that works in comparison to molybdenum disulfide (MoS_2) is tungsten disulfide (WS_2). While the valence band energy of WS_2 is higher than that of MoS_2, so is the conduction band energy. The result gives a comparable band gap to MoS_2 at ~1.3 eV as bulk crystal and ~2.1 eV as a monolayer[25]. However, with a slightly larger splitting, it should have a slightly larger band gap than MoS_2 making it an even better material for electronic devices. Another benefit of WS_2 is that the higher PL emission efficiency[28] could potentially lead to unique heterostructures with adaptive optical and electrical functions.[19,63]

As was shown with mechanical exfoliation of graphene and MoS_2, mechanically exfoliated WS_2 has also shown greater efficiency compared to its bottom-up grown counterpart. Different CVD approaches to growing WS_2 are also similar to those of MoS_2, and include the reaction of tungsten (VI) oxide (WO_3) with sulfur,[64] sulfurization of thermally deposited tungsten oxide films,[65,66] pre-dipping into a WO_3-IPA (isopropyl alcohol) solution,[67] iodine transport of WS_2,[68] and metal-organic CVD[53].

It has been shown that single layer CVD-grown WS_2 has a relatively low mobility, ~0.01 $cm^2\ V^{-1}\ s^{-1}$ compared to MoS_2,[46] leaving much room for improvements and optimizations in its performance. While there have been improvements in the mobility using other techniques such as atomic layer deposition (ALD) to raise the mobility up to 3.9 $cm^2\ V^{-1}\ s^{-1}$,[69] CVD-growth still lacks drastically in comparison. The largest mobilities recorded for any WS_2 come from the thin layered version at 8~10 nm with the largest being 234 $cm^2\ V^{-1}\ s^{-1}$.[70]

Experimental Procedure

WS_2 crystals were grown on p-doped silicon substrates covered with 300-nm-thick SiO_2. The substrate was cleaned for 10 minutes in acetone, 10 minutes in deionized water, and 10 minutes in 2-propanol before treatment with an UV ozone cleaner, ProCleaner^{TM} Plus system for 30 minutes. Once the substrate is clean, 2-3 mg of tungsten (VI) oxide (99.995%, Sigma Aldrich) was placed into the center of a clean 40-mm quartz boat. The substrate (~2 x 2 cm^2) was placed with the SiO_2 layer facing toward the tungsten source (face-down) with one edge aligned at the center of WO_3. The quartz boat was then loaded into a 2-inch quartz tube in a Lindberg Blue M tube furnace.

The system was flushed with argon and the growth procedure was performed under vacuum with 100 sccm of argon flowing throughout the growth procedure at 1.5-2.0 Torr. The CVD procedure starts as the temperature goes up to 300 ℃ over 30 minutes, remains at 300 ℃ for 30 minutes, then climbs to 550 ℃ over 30 minutes to remove any water or surface contaminates that remained after cleaning. At 550 ℃ the temperature climbs to 1100 ℃ over 15 minutes, remains at 1100 ℃ for 10 minutes, and then is cooled normally until 420 ℃ before opening the furnace to cool back to room temperature.

The initial CVD is meant to deposit a very small amount of WO_3 on the surface of the Si/SiO_2. A second CVD is needed to ensure growth of the WS_2. Once the CVD finishes, the substrate is placed into the center of a different clean quartz boat of the same size and loaded into a new 2-inch quartz tube set in the furnace. A third quartz boat was then prepared with 40 mg of sulfur (99.998%, Sigma Aldrich) and placed ~35 cm upstream of the center of the substrate, over the center of a hotplate.

The system was flushed with argon three times and the growth procedure was performed at atmospheric pressure with 100 sccm of argon flowing throughout the growth procedure. The CVD procedure starts as the temperature goes up to 300 ℃ over 30 minutes, remains at 300 ℃ for 30 minutes, then climbs to 550 ℃ over 30 minutes to remove any water or surface contaminates that remained after cleaning. At 550 ℃ the temperature climbs to 805 ℃ over 10 minutes and remains at 805 ℃ for 5 minutes. The system begins to slowly cool back down to 550 ℃ over 40 minutes, finally being cooled normally until 380 ℃ before opening the furnace to cool back to room temperature. Sulfur was introduced 2 minutes prior to the start of cooling, while the furnace is still at 805 ℃. For all measurements taken see previous section for equipment, except for the SEM in which case a Zeiss Supra 40 field-emission scanning electron microscope using an in-lens detector at the accelerating voltage of 5 kV was used instead of a Hitachi S4700 field emission scanning electron microscope in secondary electron detection mode.

Results and Discussion

A number of initial attempts to grow WS_2 by CVD were unsuccessful. The most likely reason was due to a deprivation of available tungsten during previous synthesis attempts. Initial attempts at WS_2 were done similarly to the MoS_2 procedure mentioned in the previous chapter and there was no/very poor WO_3 evaporation to the substrate leading to no appreciable growth. A secondary method was adapted where the WO_3 was placed directly onto the substrate itself for the synthesis to occur without evaporation, again leading to no growth. The difference this time was likely due to too much oxide on the substrate, inhibiting the growth when reacting with the sulfur and no proper adhesion to

the surface. This lead to limiting the amount of oxide used and after numerous trials, maximum heat was used in order to evaporate enough tungsten for the reaction to occur, while limiting the amount of oxide used.

As in the case of MoS_2, triangular islands are also the preferred morphology of WS_2 (Figure 9a). Other shapes seen in certain areas of the substrate are stars, hexagons and merging islands, are shown in Figure 9b,c. Similarly, star shapes are seen when the cool down time was too short and the reaction was not given enough time to grow, while hexagons or merging islands are due to the over-deposition of the oxide. We tried to investigate the deposition of the oxide after the initial CVD using only WO_3 by taking a Raman map, Figure 10, but after the second growth, the relationship between oxide deposition and WS_2 islands growth was unclear. As sulfurization is occurring, there is the possibility of tungsten migrating further downstream and being redeposited elsewhere. Thus far, all cases have been similar to the one shown in Figure 10 with areas of WO_3 present, without WS_2 growth. We are still considering how the growth of WS_2 relates to that of WO_3 pre-deposited on the surface but it does not currently pose much of an issue as large areas of monolayer triangular islands are forming.

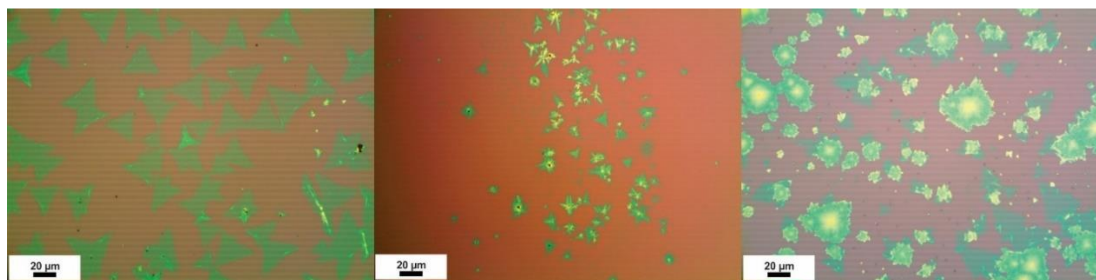

Figure 9 Differing shapes of WS_2 islands in the form of triangles (left), stars (middle) and merging islands (right).

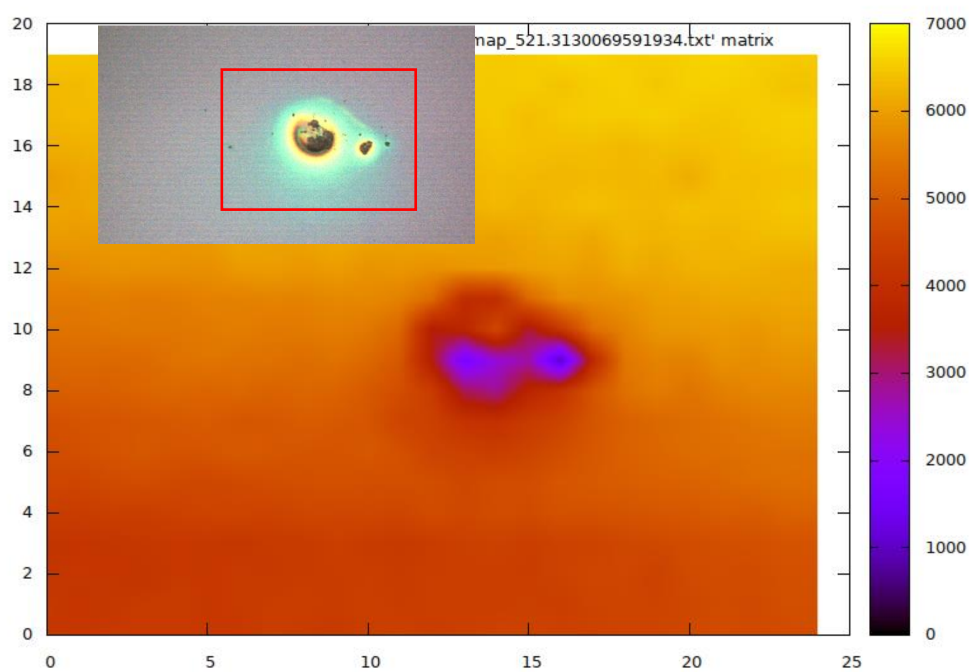

Figure 10 Raman map collected at 521 cm^{-1} of the area enclosed in a red rectangle shown in the inset.

Subtle differences between MoS_2 and WS_2 is the mechanism of growth, although it is more common for synthesis of many materials to occur at multiple nucleation points we do not necessarily see that in the MoS_2 growth very often but in the case of WS_2 it is far more common. For many trials, it is possible to see multiple small triangular islands forming on the original monolayer, Figure 11. Since there are multiple nucleation sites, it makes monolayer growth more difficult given that the focus has been to grow it off a single nucleation site without a seed present, to compare the results properly to those of MoS_2. Unfortunately, we are not able to observe the growth process directly in our furnace via SEM, transmission electron microscopy (TEM), or even optical microscopy. It can be said that many of the monolayers grow from a single nucleation site because the triangular shape appears unobstructed at the edges, see Figure 9a. This would mean that the nucleation sites appearing on top of the monolayer are due to defects such as dislocations or out-of-plane interstitial atoms that occur during the growth procedure. These are caused by an excess sulfur or contact with unreacted WO_3, creating an additional site for nucleation to adsorb to.

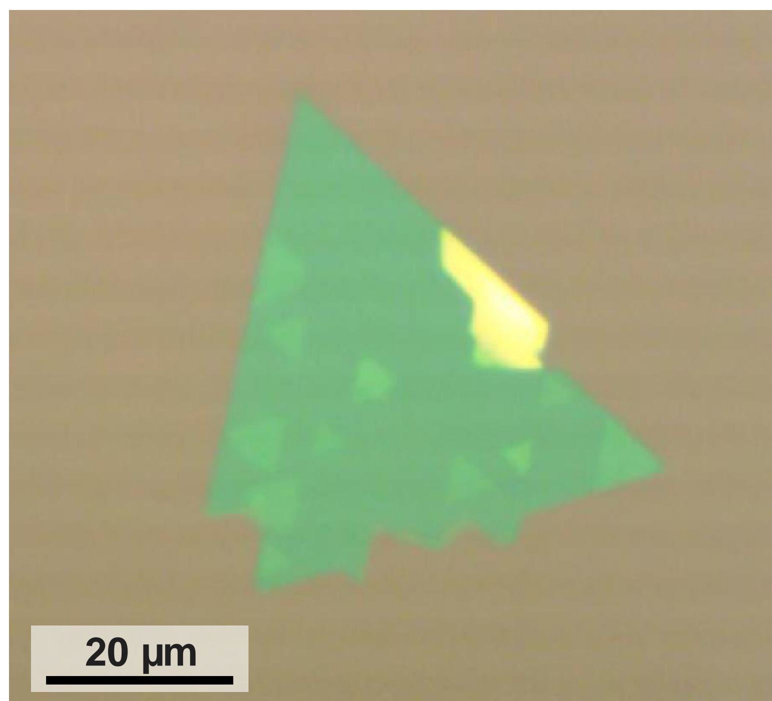

Figure 11 Multiple nucleation sites on the surface of a WS_2 crystal.

To determine if WS_2 was grown, Raman spectroscopy allows for fast and easy determination of results. Figure 12 shows the Raman spectra of a uniform single layer WS_2 crystal as grown by the reported procedure seen in the 'inset' closely matching that of reported literature.[66,69] The difference in shifts is caused by lasers of different wavelength. Raman spectra of different samples had revealed a difference between the A_{1g} peak and the 2LA(M) peak increasing from monolayer to bulk, 65.58 to 70.39 cm^{-1}, respectively. Another indicator is that the peak at 347 cm^{-1} has a much greater relative intensity than the peak at 413 cm^{-1}.

AFM was the second characterization technique used to determine the heights of the islands. It was found that the height was ~1 nm, which matches with previously reported results[69]. With higher adsorption of sulfur to the oxide than was seen in MoS_2, it is also more common to see some thicker islands form farthest upstream (closest to the sulfur source). These crystals are much thicker than what was seen in the trilayer growth of MoS_2. AFM of these thicker crystals confirmed that the heights were 8~20 nm (Figure 13).

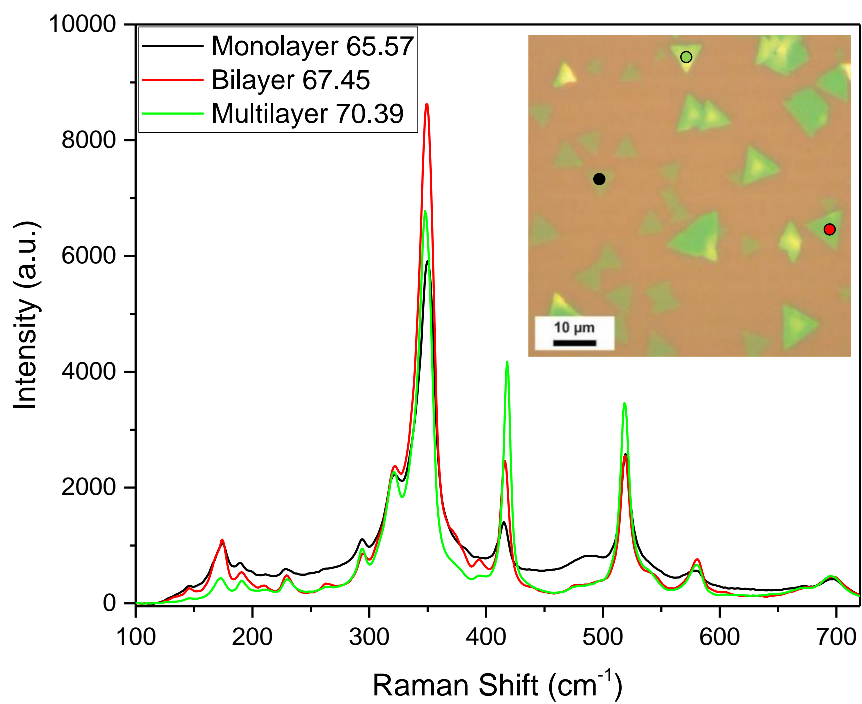

Figure 12 Raman spectra of monolayer (1L), bilayer (2L) and multilayer (ML) WS_2 crystals shown in the inset.

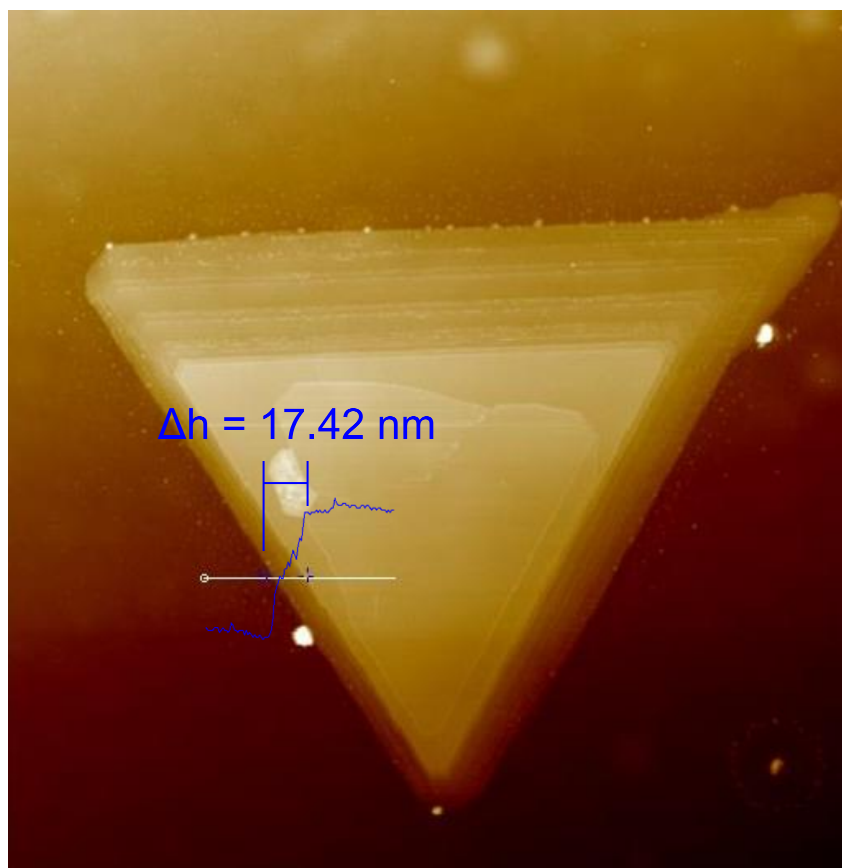

Figure 13 AFM showing the height of a thick multilayer WS_2 crystal closest to the sulfur source. Change in vertical height (Δh).

Finally, the electronic properties of the single layer WS_2 crystals were measured. The device seen in Figure 14 was one of the better devices fabricated. The mobility was found to be moderately low in comparison to MoS_2, Figure 14. Although the mobility is ~0.20 $cm^2 V^{-1} s^{-1}$, it is almost 20 times that of reported values for CVD grown WS_2, which were not reported to be any higher than 0.01 $cm^2 V^{-1} s^{-1}$.[46] However, a number of fabricated devices were nonfunctional due to the degradation of the SiO_2 substrate, since its melting point is close to that of WO_3. The degradation of the substrate was associated with the formation of nanoscopic holes, which caused high leakage currents and failure of the devices. Transferring the WS_2 flakes to a new substrate that was not subjected to high temperature can drastically reduce leakage current. However, a new set of transfer related defects can be introduced, such as trapping of transfer liquid or particles, leading to mobility reduction. The measured mobilities are still higher than what has been reported.

In the future, transfer of the monolayer WS_2 to a new substrate lacking holes should help to ensure a larger sample size. While the growth modifications have not drastically increased the mobilities, the results are encouraging as far as CVD grown WS_2 is concerned. The gap between CVD synthesis and exfoliation techniques is shrinking. Additionally, our two-part synthesis leads to appreciable monolayer growth, without the requirement of a seed catalyst. In summary, WS_2 synthesis still has much to improve upon but with the limited data acquired, it is applicable towards more complex structures.

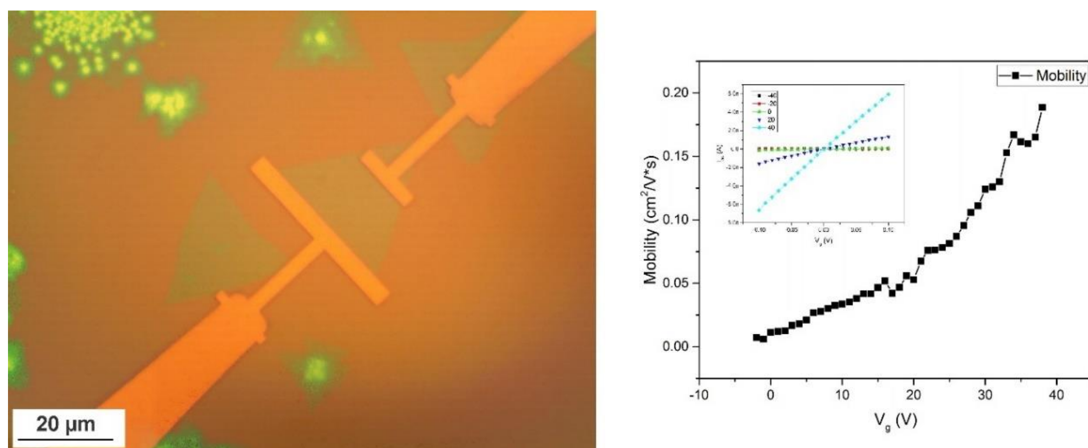

Figure 14 Optical image of single layer WS_2 device (left). Mobility of WS_2 device (right) with an inset showing I_{DS}-V_{SD} dependencies measured at different gate voltages from -40 V to 40 V with a 20 V step.

CHAPTER 3: HETEROSTRUCTURES OF 2D MATERIALS

In recent years, there was a growing interest of heterostructures of 2D materials. Stacking is one method of combining different 2D materials to form a heterostructure with distinct properties. Stacking can be realized for materials obtained from both a top-down or bottom-up approaches.

Many top-down methods involve individual exfoliation of the 2D materials, prior to stacking, and then flakes are transferred one on top of another. The van der Waals forces that hold graphene and other TMD materials together are strong enough that by placing them in contact with one another they will not move. Some of the various methods of mechanical transfer involve the use of polymers[71,72] to lift one material off from its substrate. Using some form of micromanipulator, the flake chosen for transfer can then be placed at the desired location. After aligning the flake with a proper orientation and position under an optical microscope or other objective lens, the flakes can be brought together. This method also allows the freedom to change the alignment of the materials and observe how different configurations change the interaction of the two layers.[73] Washing away of polymers is not a perfect process which leaves behind trace amounts that will hinder further building. Recently, more advanced dry peel-off methods have started to emerge to eliminate the use of polymers for such transfers.[74–76]

Bottom-up growth approaches are much more versatile in the number of techniques available, ranging from CVD,[77] pulsed laser deposition (PLD),[78] vapor-liquid-solid mechanism(VLS),[79,80] atomic layer deposition (ALD),[81] and others, provide a large variety 2D materials that can be combined in various heterostructures. Currently, CVD growth of 2D materials is mostly limited by the sensitivity of growth conditions used

since most have different growth parameters. While the bottom-up approaches are more diverse, the top-down mechanical exfoliation is readily accessible as long as the bulk crystals themselves are available.

Heterostructures do not necessarily need to be stacked vertically as described in the above methods, but can also fused horizontally using the bottom-up approach. The ability to create a structure without gaps between two materials or using a top-layer to bridge two materials is a more recently developing idea.[82] Many electronic properties are determined by the edge of a material, which means that if that interface can be altered or added to, so should the electronic properties.[3,83] In this chapter, different forms of heterostructures will be looked at via top-down and bottom-up approaches, while not directly comparing the two methods on the same materials. Much of the following work lays a foundation to grow and expand upon.

3.1 Graphene on boron nitride

Introduction

The field of graphene has seen more work done on it in recent years than most other forms of research, but still many new ideas are still being generated as for its uses or how to improve its current uses. The problems with many graphene devices on silicon oxide (SiO_2) are surface defects leading to disordered structure, charge trappings that can cause shifts in the Dirac point,[84] and impurity scattering.[4] In order to remove surface defects and help reduce charge trappings from the graphene it was thought to transfer the graphene onto hexagonal boron nitride which is atomically smooth and free of dangling bonds.[12] Boron nitride has great thermal and dielectric stability,[85] which will greatly help to support properties of another material rather than inhibit them. Some of the issues with

transferring graphene onto different structures are polymer residues and the appearance of wrinkles that develop due to the relaxation of the polymer once graphene has been removed from the substrate.[86] Different ideas have emerged to try and counter these wrinkles, which involve either applying a thicker/secondary layer of polymer[86] or using a second polymer with more rigidity to it.[72]

Upon setting graphene atop boron nitride, the van der Waals interactions between the two materials is strong enough to hold graphene in place. While the interactions are strong, they are not as strong as the interactions that hold the bulk crystals of each materials together due to lattice mismatching that is accommodated for by the van der Waals gap.[87,88] These van der Waals structures have been looked to expand graphene's uses beyond current limitations like it's zero band gap[89] and increasing its mobility.[90] Overcoming these limitations, could result in more sophisticated electronic devices.

In this study, the goal was to first create a functional graphene boron nitride field effect transistor, then study the functionalization of graphene on an insulator compared to graphene on just SiO_2. The second goal is to compare the same graphene flake placed on top of boron nitride and on the SiO_2 substrate. The second goal will help to ensure that regardless of the material used, the properties demonstrated by that material will change.

Experimental Methods

Graphite flakes (Sigma Aldrich) were first exfoliated several times using Scotch tape. Once determined to be thin enough, the tape was pressed onto p-doped silicon substrates covered with a 300-nm-thick SiO_2. The substrate was then heated to help improve the adhesion of large area graphene flakes[91] and then slowly peeled off. An optical microscope was used to approximate the number of layers of graphene based

upon transparency and color. If a flake is thought to be single layer or of few layers, a Raman spectrum was measured to confirm the number of layers, as Raman spectra of single to few layer graphene has been well documented[92–95] and can be quickly cross referenced.

Polymethyl methacrylate in 4% anisole (PMMA-A4) was then drop-cast on the substrate and spin coated on an SH-2 Magnetic Stirrer for 5 minutes at the max rate. After spin coating, ~1 cm of PMMA was removed by scratching with a razor blade at the edges furthest from the desired graphene flake to help later dissolve PMMA[72]. A piece of PDMS is then cut to be slightly larger than the substrate and small holes are pierced near the edges of the two sides that will line up with the areas of PMMA and exposed substrate that were removed. These holes will help allow solvent to get under the PDMS and dissolve the PMMA more easily as well as act as alignment markers once the graphene has been removed from the substrate. The PDMS was then placed over the PMMA as indicated above and gently pressed to ensure adhesion takes place evenly. The PDMS/PMMA/graphene/substrate should then be placed directly into a 10% KOH solution with the PDMS on top. After a short while the SiO_2 will begin to dissolve, releasing the PDMS/PMMA/graphene to be left floating on top of the solution. The substrate can be safely picked up with tweezers at the corner of PDMS with holes to avoid damaging desired graphene flake. It was then washed with water three times to wash off most the remaining KOH leftover from the solution. The sample was then set on a glass slide with the PDMS side in contact with glass to allow the sample to dry.

While the sample dries, a large yet thin boron nitride flake (Momentive) then needs to be exfoliated in the same manner as graphene, indicated above. The major

difference is that it is more difficult to determine the thickness of boron nitride since there has not been enough Raman work done to determine the thickness by differing Raman wavenumbers, only shifts relating thin layers to bulk are generally seen.[96] As a fallback, AFM can then be used to determine thickness of boron nitride. While the boron nitride does not necessarily need to be single layer for most of the goals of our experiments, allowing for some leeway in thickness, but does need to be uniformly thick. After confirmation of the thickness of the desired flake it was centered and refocused under an optical microscope. Using a camera and TopView program, the flake can be outlined to record the position and lowered out of focus without disturbing the x/y axial stage controls.

Once the PDMS/PMMA/graphene was dry, the glass slide can then be attached inverted to a secondary stage that has the capabilities to move in the x, y and z directions. The graphene flake was focused using the secondary stage controls and shifted into the outline of the boron nitride flake previously recorded in the program. Once the secondary stage has been set into the outline, the microscope stage can then be raised slowly and steadily, to not shift the x/y position. Upon contact of the substrate containing the boron nitride flake and the glass slide holding PDMS/PMMA/graphene the stage should be continued to be raised to promote better adhesion between the substrate and PMMA. After 5 minutes the secondary stage was slowly raised to lift the substrate from the microscope stage. The microscope stage can again be lowered out of focus and the secondary stage refocused to determine if the graphene was in fact placed onto the boron nitride. The secondary stage can then be moved and the sample lowered onto a hotplate at 65 ºC for 10 minutes to ensure better adhesion between the graphene and boron nitride.

After heating the sample is removed from the secondary stage and left to cool slowly back to room temperature. The sample is finally washed with acetone to dissolve the PMMA and release the graphene onto the boron nitride. Characterization of the van der Waals heterostructure created is done by optical microscopy, Raman microscopy, atomic force microscopy (AFM), and scanning electron microcopy (SEM).

Results and Discussion

Successful transfer of graphene onto boron nitride is shown in Figure 15. The graphene in this sample is not single layer but demonstrates a perfectly fit graphene transfer and how the finished product should look. Because the graphene is completely isolated from the Si/SiO_2 substrate, that eliminating any potential surface interactions with SiO_2. Figure 16a and b show two different single layer graphene flakes on the same piece of boron nitride and Figure 16c shows a third single layer graphene flake on the SiO_2 ~200 µm away from the boron nitride flake. The transfer characteristics and mobilities of each graphene flake are shown in Figures 16d-e. The graphene flakes that are on boron nitride show Dirac points very close to zero whereas the graphene flake on SiO_2 shows a Dirac point that is drastically shifted away from zero. Since these flakes were prepared on the same substrate at the same time there should be no difference in how the devices were prepared meaning the boron nitride is eliminating charge trappings on the surface.

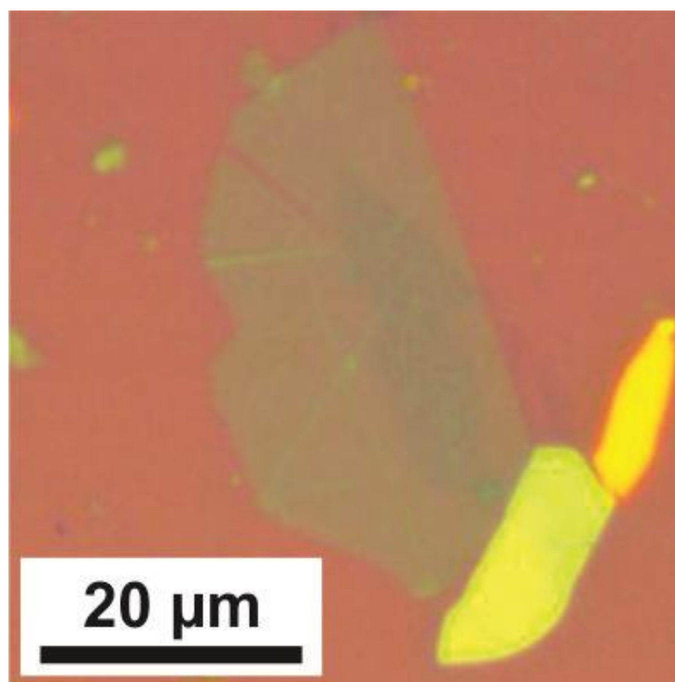

Figure 15 Few-layer graphene on boron nitride.

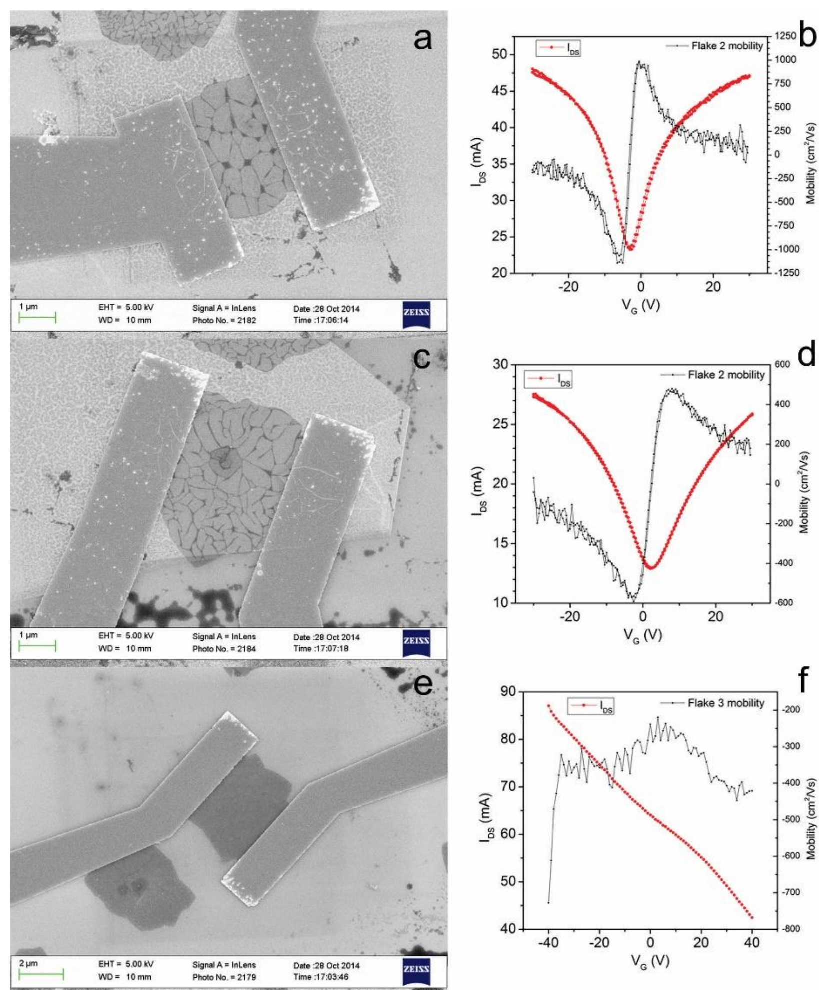

Figure 16 Single layer graphene devices with transfer characteristics and mobilities from -40 V to 40 V. (a and c) Graphene on boron nitride and (e) graphene on SiO_2. (b) Transfer characteristics of (a) showing a Dirac point around -3 V. (d) Transfer characteristics of (b) showing a Dirac point around 3V. (f) Transfer characteristics of (e) showing a Dirac point outside of the measured range.

If a device is positioned so that the area between the electrodes is completely on boron nitride the results should be the same. Figure 17a shows a finished device where the graphene was not completely placed fully on the boron nitride flake but the device that was fabricated only measures the area between the graphene that is atop the boron nitride. The mobility of the device can be seen to be ~2500 $cm^2 V^{-1} s^{-1}$, Figure 17d. (This sample is not single layer graphene but few-layers. The measurements show reasonable mobility for a few-layered device.) The next step after having created a FET of graphene on boron nitride would be to then functionalize it since the Dirac point remains closer to zero than that of flakes on SiO_2 (Figure 16) helping to standardize shifts of different functional groups. Since most devices are unable to attain a Dirac point at or near zero on SiO_2 then the shift of a Dirac point due to functionalization might result more from the functional group affecting the SiO_2 than the flakes in question.

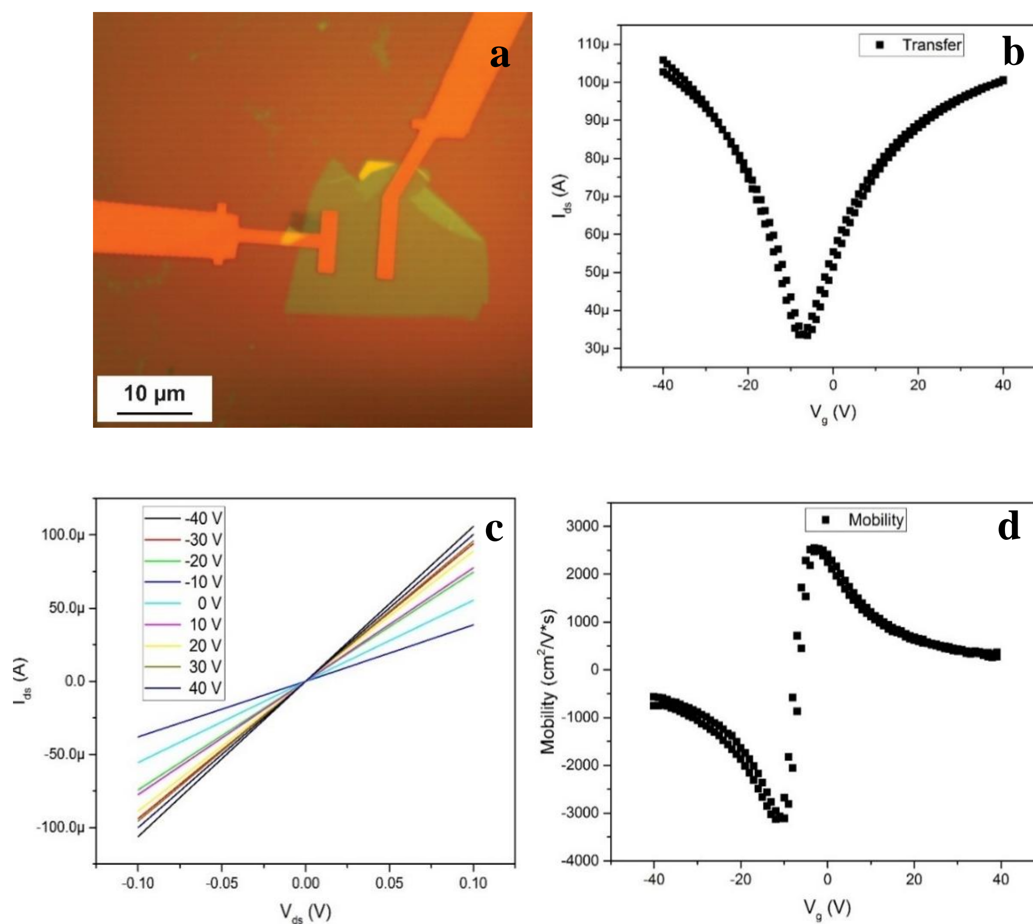

Figure 17 Few-layer graphene device on boron nitride. (a) Optical image. (b) Transfer characteristics of MoS_2 device shown in (a). (c) I_{SD}-V_{SD} dependencies measured at different gate voltages ranging from -40 V to 40 V with a 10 V step. (d) Mobility calculation based on the transfer characteristics shown above.

While many studies have looked at the increase in electrical properties from placing graphene onto boron nitride,[12,97,98] there has been very little work done demonstrating that difference using the exact same graphene flake. To make such a comparison, a very long piece of few layer graphene (196 µm) was set on both boron nitride and lead zirconate titanate (PZT). Two devices were fabricated using the same graphene flake, as shown in Figure 18c and d. Figure 19 demonstrates how the electrical properties changes from placing the device on boron nitride/PZT compared to being left on the PZT. Because the boron nitride flake being used in this sample is so thick, it is eliminating the hysteresis seen from switching of the PZT in graphene on PZT. It can be seen that the drain-source current of graphene on boron nitride is also increased by a factor of ~4, which relates to the graphene on boron nitride shown above in Figure 17 having similar drain-source current.

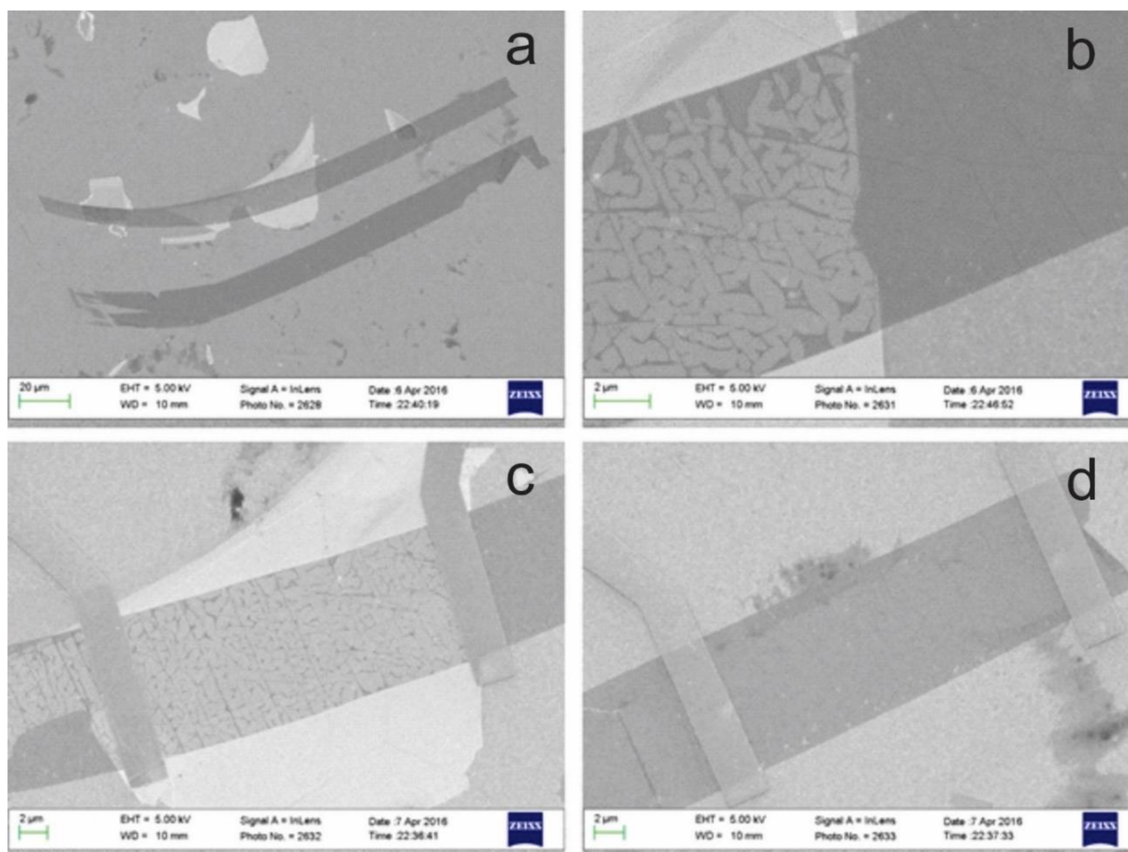

Figure 18 (a) Few-layer graphene on both boron nitride and PZT. (b) Enlarged area of (a) showing the difference between the graphene on boron nitride/PZT (left portion) and just PZT (right portion). Device fabricated of the graphene on (c) boron nitride/PZT. and (d) PZT.

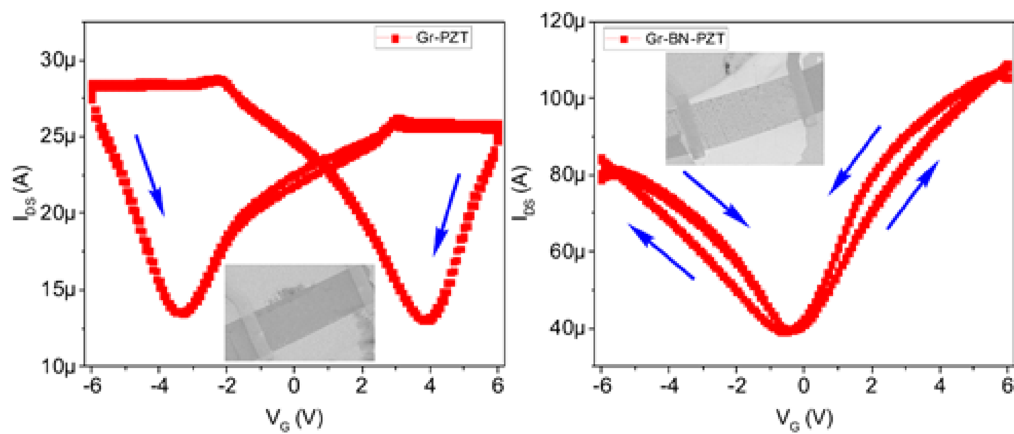

Figure 19 Transfer characteristics of Gr-PZT (left) and Gr-BN-PZT (right), where Gr stands for graphene and BN stands for boron nitride.

Future work would entail the addition of a second boron nitride flake on top of the graphene already on boron nitride to act as a top-gate, that can be used in place of a band gap to control switching[99]. Using the same procedure listed in the experimental section for graphene transfer, the same was attempted for boron nitride. Figure 20 shows the first completed sample of a boron nitride/graphene/boron nitride sample. As a preliminary result, the structure shows the appearance of new wrinkles not previously seen after the second transfer of boron nitride. This is likely due to liquids being trapped between each set of layers as the wrinkles were not seen prior to lift off of the polymer. This effect has also been seen in just the single transfer if washed or sonicated with an excess of acetone when removing PMMA. It is not clear as to why acetone can get trapped in between layers so easily during transfer of boron nitride but since graphene excels at preventing liquids moving through it, it could help explain why so much liquid becomes trapped after it squeezes between the layers. To determine if this preliminary result could lead to better stability or lower operating voltages, a top-gate FET has been fabricated on the graphene and the top boron nitride flake. The Dirac point of the materials is still close to zero, seen here to be about -2 V, indicating less surface charge trappings that were seen on SiO_2. As seen in Figure 20, from -5 V to 5 V, a large hysteresis occurs similar to the previous example where graphene was placed onto PZT. The BN/graphene/BN heterostructures find emerging applications in high-performance nanoscale optoelectronics,[100] as well as flexible and transparent electronics.[101]

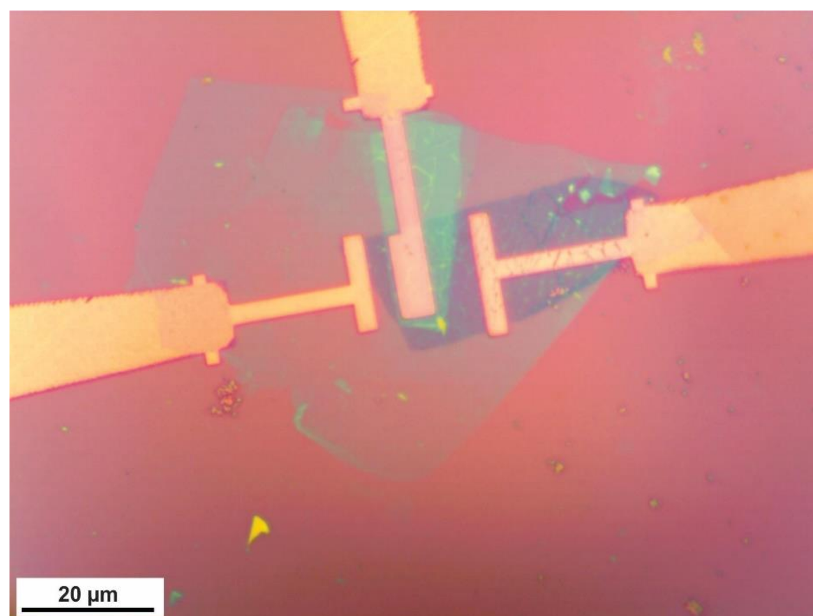

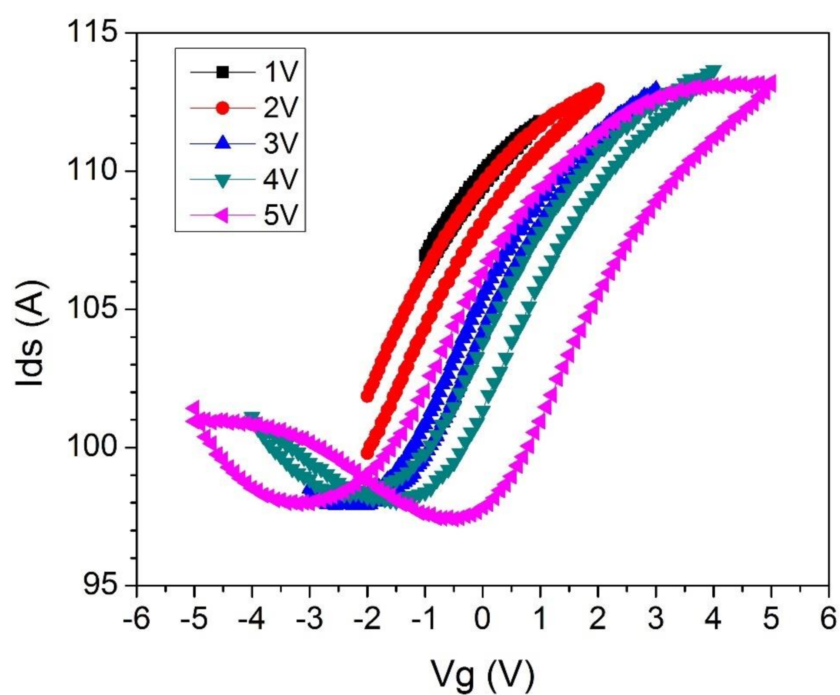

Figure 20 A second layer of boron nitride placed on top of the graphene previously laid upon a boron nitride flake with a top-gate FET (top). Transfer characteristics of the device shown above at different voltages ranging from -1 V to 1 V through -5 V to 5 V (bottom).

3.2 Molybdenum disulfide on boron nitride

Introduction

With the work already completed on molybdenum disulfide (MoS_2) discussed in previous chapters and the work described in the previous section, the next step for MoS_2 is to grow it on top of boron nitride. The idea is like that of placing graphene on top of boron nitride to enhance the mobility[90] and eliminate charge trapping.[84] Similar work has already been done with the exfoliation of MoS_2 onto boron nitride, some going even further of making a FET of these structures having graphene as the gate electrode demonstrating larger mobilities[101,102]. The reduction of surface defects for growing MoS_2 is also idealized by using boron nitride, since it is atomically flat and has very few dangling bonds.[12] It is unclear how many layers of boron nitride it should take to screen the charged defects on the surface of SiO_2. As such, it is reasonable to have a different number of layers present on the same flake to determine at which layer the defects can be screened. Another reason that boron nitride was chosen besides the previous work done is due to its triangular growth mechanism seen when it is grown in smaller areas via CVD.[103] If both grow triangularly, the boron nitride should have a similar hexagonal lattice to that of MoS_2 allowing for more relaxed growth if the sizes of the unit cells are compatible.

While CVD has become a promising route to explore new materials and their growth patterns, there are still many different combinations of materials still undeveloped or underdeveloped. A similar example to the work presented here can be seen in the work of Dmitry Ruzmetov *et al*. on “Epitaxial Molybdenum Disulfide and Gallium Nitride,” where they present similar results done on gallium nitride rather than boron nitride.[104]

Mitsuhiro Okada *et al*. report another experiment like our own using tungsten rather than molybdenum to grow tungsten disulfide on boron nitride.[105] In this section, we present work reflecting the previously mentioned studies using our own techniques developed previously and to the best of our knowledge, on a combination of semiconductor/insulator materials not yet worked upon using the direct growth of the semiconductor in CVD onto the insulating material.

Experimental Procedure

A substrate (~2 x 2 cm^2) was cleaned for 10 minutes in acetone, 10 minutes in deionized water, and 10 minutes in 2-propanol before treated with an UV ozone cleaner, ProCleaner™ Plus system for 30 minutes. Boron nitride (Momentive) was then exfoliated several times using adhesive tape. Once the flakes were determined to be thin enough, the tape was pressed onto p-doped silicon substrates covered with 300 nm-thick SiO_2. The substrate was then heated to help improve the adhesion of larger area flakes[91] and then slowly peeled off. Flakes were first scrutinized using an optical microscope to determine which flakes might be thin enough or contain enough different steps with enough space to grow good single layer MoS_2 triangles. The heights were then determined using AFM before CVD could be done to ensure accurate height profiles of thin layered boron nitride. This process was repeated twice onto smaller substrates (1 x 0.25 cm^2).

Once the substrates contain good boron nitride flakes, 0.5-1 mg of molybdenum (VI) oxide (99.5%, Sigma Aldrich) was placed into the center of a clean 40-mm quartz boat. One of the smaller substrates (1 x 0.25 cm^2) was placed with the SiO_2 layer facing away from the MoO_3 (designated face-up) directly over the center of the MoO_3 and the second small substrate placed in the same orientation just downfield of the first. The

larger substrate (~2 x 2 cm^2) was placed with the SiO_2 layer facing toward the MoO_3 (face-down) with one edge aligned over center of the MoO_3. The quartz boat was then loaded into a 2-inch quartz tube in a Lindberg Blue M tube furnace. A second quartz boat was prepared with 50 mg of sulfur (99.998%, Sigma Aldrich) and placed ~35 cm upstream of the MoO_3, over the center of a hotplate.

The system was flushed with argon for 5 minutes and the growth procedure was performed at atmospheric pressure with 100 sccm of argon flowing throughout the growth procedure. The CVD procedure begins as the temperature goes up to 300 ℃ over 30 minutes, remains at 300 ℃ for 30 minutes, then climbs to 550 ℃ over 30 minutes to remove any water or surface contaminates that remained after cleaning. At 550 ℃ the temperature climbs to 805 ℃ over 10 minutes, remains at 805 ℃ for 5 minutes. The cooling processes then begins with the furnace dropping to 550 ℃ over 30 minutes finally allowed to cool normally until 380 ℃ before opening the furnace to cool back to room temperature. To produce single layer MoS_2 on boron nitride, the hotplate should be turned to 250 ℃ 2 minutes before the cooling process begins while still at 805 ℃.

Atomic force microscopy images were recorded using a Bruker Dimension Icon atomic force microscope. Raman spectroscopy was performed using a Thermo Scientific DXR Raman microscope with a 532 nm laser. Scanning electron microscopy (SEM) images were taken using a Zeiss Supra 40 field-emission scanning electron microscope using an in-lens detector at the accelerating voltage of 5 kV.

Results and Discussion

The growth procedure for MoS_2 on SiO_2 does not translate as well as initially thought and thus leading to a slightly different experimental procedure than used in

Chapter 1. This is likely due to the differences in surfaces and nucleation. SiO_2 was clean and only contained surface defects. The nucleation of MoS_2 could be anywhere and it was not confined. Wafer scale films were not seen from the procedure described in Chapter 1. In the case of boron nitride both of these details were an issue. The larger problem of the two was the nucleation sites, because having flakes of boron nitride will instantly generate multiple nucleation sites at the edges, whether it be between the SiO_2 and a flake of boron nitride or individual layers of boron nitride within the same flake. As can be seen from the optical image in Figure 21, the green area around the boron nitride crystal (yellow) shows much more nucleation around the edges of the flake than other parts of the substrate. The area highlighted in red from Figure 21 shows the large clusters of nucleation between different layers. With more nucleation at edges between layers, MoS_2 also requires more space between the edges of two layers for triangular island growth to occur. These two problems lead to decreasing the amount of cooldown time to get smaller MoS_2 triangles to fit better in areas between layers but with later sulfur introduction time, *i.e.* turning the hotplate on later.

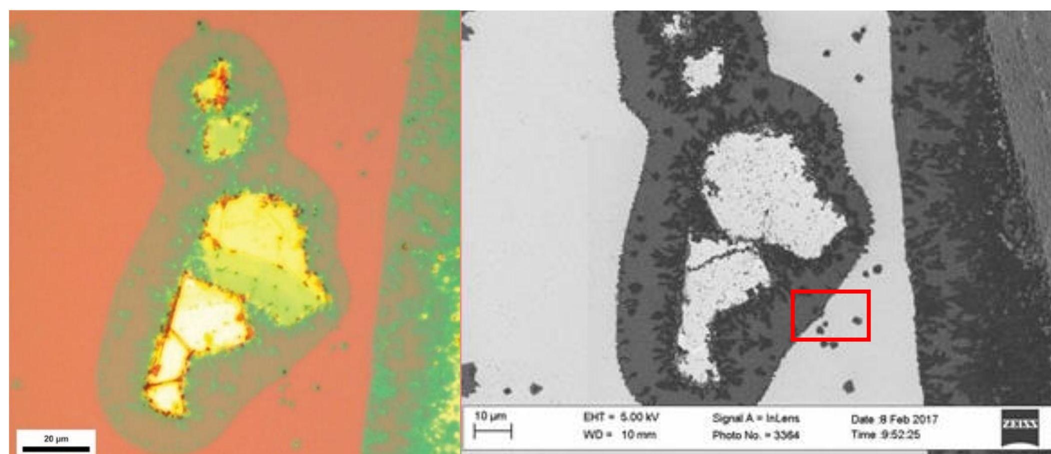

Figure 21 Optical image demonstrating MoS_2 nucleation being favored at the edges of boron nitride (left). SEM image of the optical image from the left panel of MoS_2 growth around and on top of boron nitride (right).

Since we predicted that growth should be better on boron nitride than just SiO_2, it can be reasoned that the lattice mismatch will be one of the largest contributing factor to how well MoS_2 can grow. The lattice also contributes to the directional growth of the MoS_2 on the boron nitride, it should grow in the same direction as the boron nitride's crystal structure and if it does happen epitaxial alignment should be seen consistently throughout the crystal. A representative sample of MoS_2 grown on thicker boron nitride (>100 µm) is shown in Figure 22. The origin of alignment for triangles becomes clear from the top and right edges, highlighted with a red and green line respectively. Of all the MoS_2 triangles present in Figure 22, >90% have two sides that align with both the red and green lines shown.

The samples that do not have this same type of alignment pattern are the very thin flakes of boron nitride, where surface defects of the SiO_2 could still be more impactful than the pristine surface of boron nitride. Figure 23 shows a thin boron nitride with MoS_2 grown but it does not appear epitaxially aligned like the crystals from Figure 22. A sample containing a boron nitride flake with thickness varying from very thin with unaligned regions of MoS_2 to the thicker regions of aligned growth is shown in Figure 24. The AFM image in Figure 25 shows that the triangles grown in the thicker regions are in fact single layer, which was also confirmed by Raman spectroscopy.

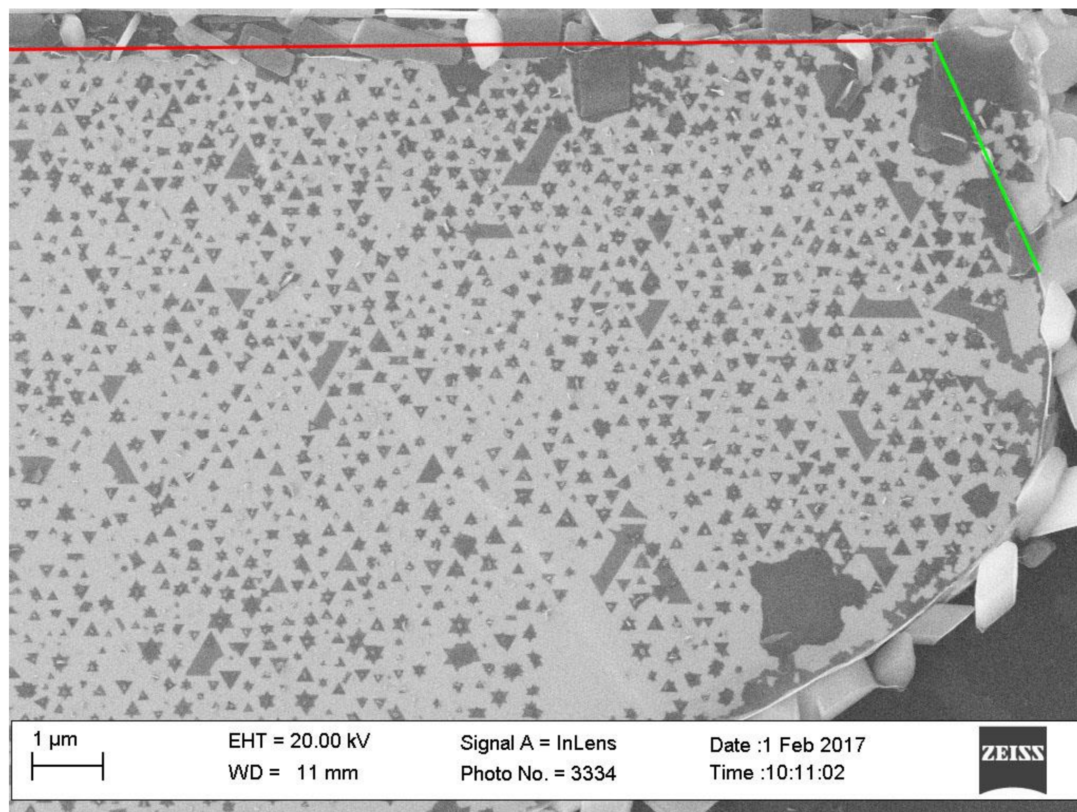

Figure 22 SEM image demonstrating the alignment of MoS_2 triangles compared to the edges of boron nitride.

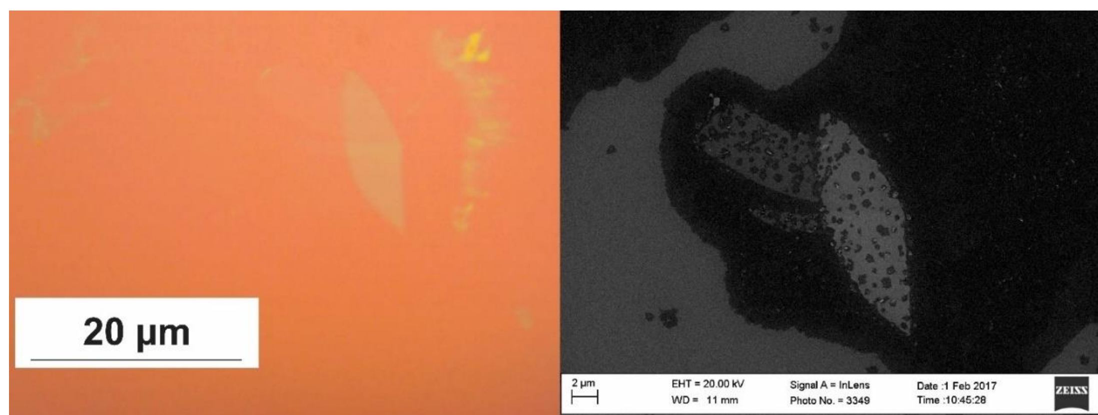

Figure 23 Optical image of very thin boron nitride flake containing multiple thicknesses of few layers prior to MoS_2 growth (left). SEM image of MoS_2 grown on/around the boron nitride flake with no epitaxial alignment or very little triangular growth seen (right).

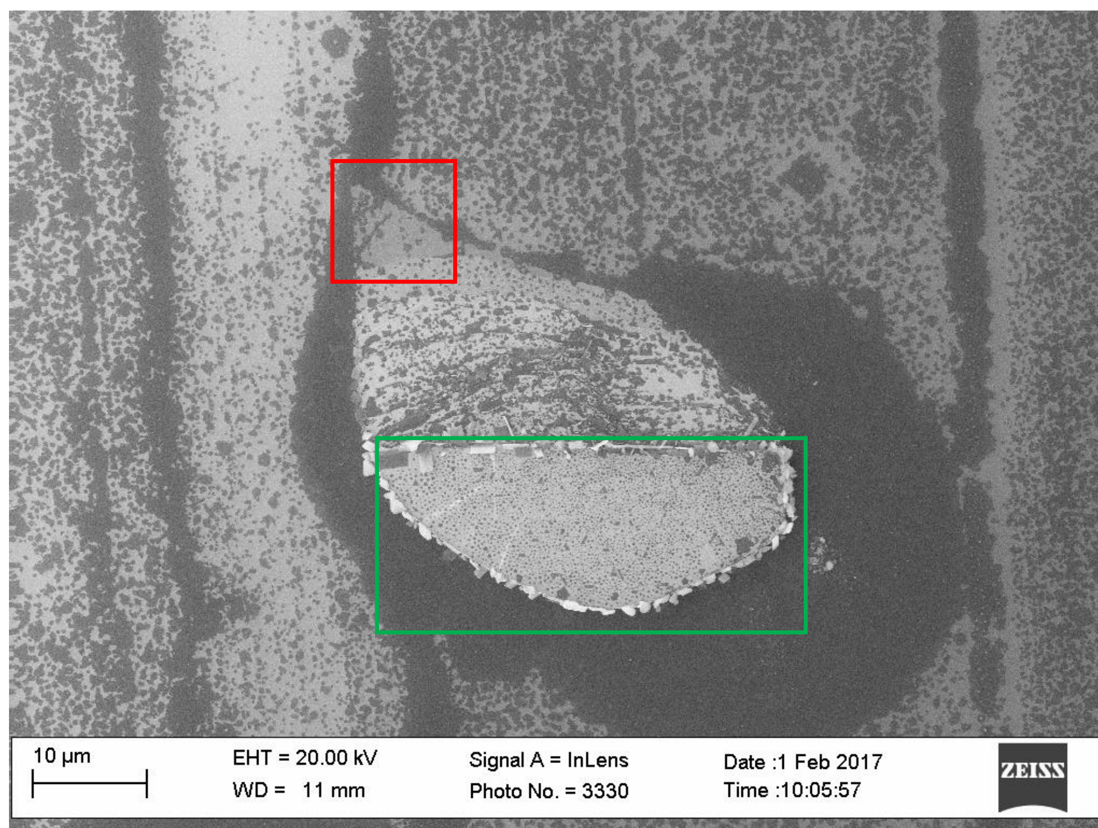

Figure 24 SEM image of boron nitride with thickness ranging from double layer (red) to greater than 100 layers (green), the thinnest parts showing no epitaxy and the thicker areas with good alignment can be seen in Figure 22.

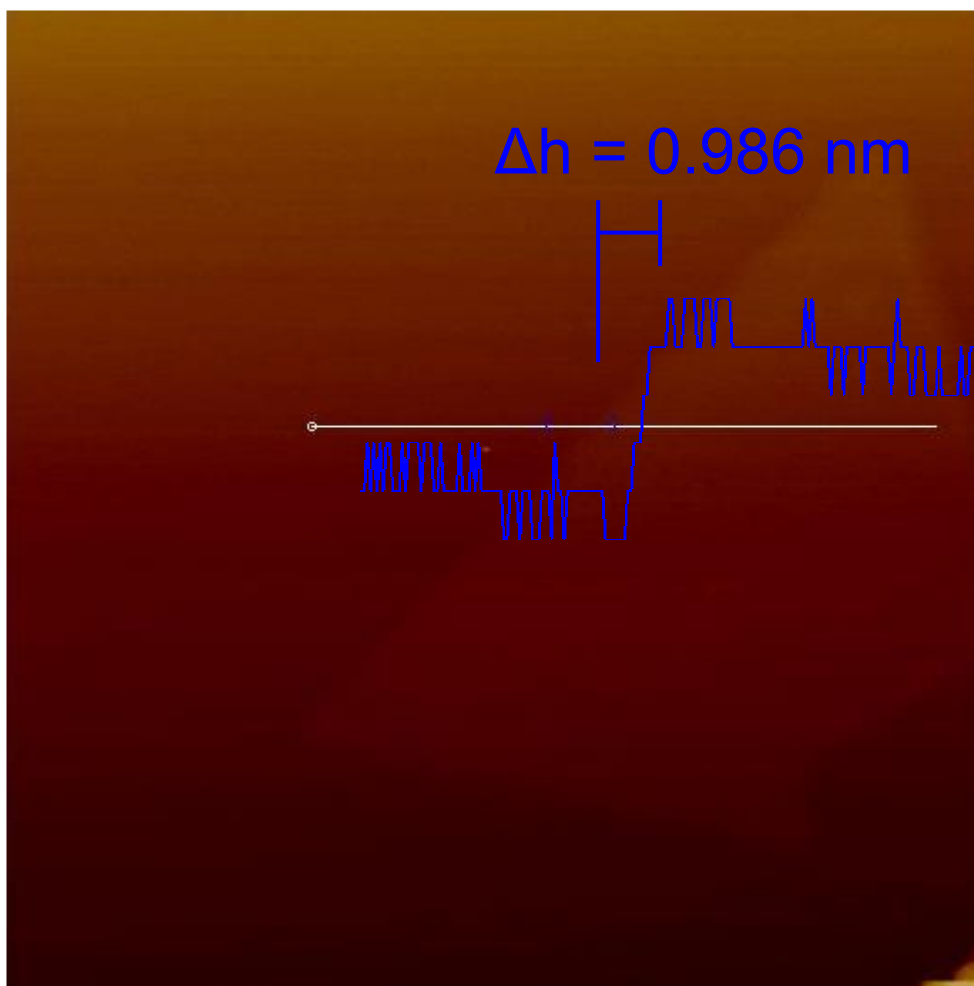

Figure 25 AFM confirming single layer MoS_2 triangles are grown in the thicker region of boron nitride. Change in vertical height (Δh).

3.3 Molybdenum disulfide/tungsten disulfide

Introduction

Strong interest TMDs and heterostructures resulted in the logical next step of combining MoS_2 and WS_2 to create new heterostructures, with unique properties, not seen in either material. While MoS_2/WS_2 heterostructures are not new, and much work has already been underway with these structures in the vertical direction, one stacked on top of the other,[98,106–109] much less has been done in the lateral direction of these two materials, in-plane with one another.[98,110,111] Many of the challenges facing the lateral heterostructures, not only MoS_2/WS_2 but others such as WS_2/WSe_2, $MoS_2/MoSe_2$ and $MoSe_2/WSe_2$ are poor interfaces,[112] lattice mismatch,[82] or special precursors to help create good contacts.[111]

Many of the aforementioned procedures have certain issues to overcome while using single-step growth techniques giving rise to the idea to use a two-step process. Having already established a two-step method for growing WS_2 using tungsten oxide deposition mentioned in Chapter 2, see experimental procedure, the foundation for heterostructures using a two-step process was already in place. Kun Chen *et al.* also used a similar idea of first growing an MoS_2 island in an initial CVD and then growing a WS_2 island around it in a second CVD to simplify the process of growing a lateral heterostructure.[110] Our idea and goal was originally to create a structure with a WS_2 island grown using the pre-deposited WO_3 to form a MoS_2 island around it during the second phase of CVD growth. While we attempt to grow both islands in the same CVD cycle, it still utilizes a different method from the single-step growth techniques which

could allow for the expansion of growth for different materials. In this section, we present findings similar to the goal previously mentioned but not with the originally desired configuration.

Experimental Procedure

MoS_2/WS_2 crystals were grown on p-doped silicon substrates covered with a 300-nm-thick SiO_2 layer. The substrate was cleaned for 10 minutes in acetone, 10 minutes in deionized water, and 10 minutes in 2-propanol before being treated in an UV ozone cleaner, ProCleaner^{TM} Plus system for 30 minutes. Once the substrate is clean, 1-2 mg of WO_3 (99.995%, Sigma Aldrich) was placed into the center of a clean 40-mm quartz boat. The substrate (~4 x 2 cm^2) was placed with the SiO_2 layer facing toward the tungsten source (face-down) with one edge aligned at the center of WO_3. The quartz boat was then loaded into a 2-inch quartz tube in a Lindberg Blue M tube furnace.

The system was flushed with argon and the growth procedure was performed under vacuum with 100 sccm of argon flowing throughout the growth procedure at 1.5-2.0 Torr. The CVD procedure starts as the temperature goes up to 300 ºC over 30 minutes, remains at 300 ºC for 30 minutes, then climbs to 550 ºC over 30 minutes to remove any water or surface contaminates that remained after cleaning. At 550 ºC the temperature climbs to 1100 ºC over 15 minutes, remains at 1100 ºC for 10 minutes, and then is cooled normally until 420 ºC before opening the furnace to cool back to room temperature.

The second CVD will be needed to ensure growth of the heterostructure of MoS_2/WS_2. Once the CVD finishes, the substrate is then placed into the center of a different clean quartz boat of the same size with 0.4-0.6 mg of MoO_3 (99.5%, Sigma

Aldrich) in the center of it then loaded into new 2-inch quartz tube set in the furnace. A third quartz boat was prepared with 40 mg of sulfur (99.998%, Sigma Aldrich) and placed ~35 cm upstream of the center of the substrate, over the center of a hotplate.

The system was flushed with argon for 5 minutes and the growth procedure was performed at atmospheric pressure with 100 sccm of argon flowing throughout the growth procedure. The CVD procedure begins as the temperature goes up to 300 ºC over 30 minutes, remains at 300 ºC for 30 minutes, then climbs to 550 ºC over 30 minutes to remove any water or surface contaminates that remained after cleaning. At 550 ºC the temperature climbs to 805 ºC over 10 minutes, remains at 805 ºC for 5 minutes. The cooling processes then begins with the furnace dropping to 550 ºC over 40 minutes finally allowed to cool normally until 380 ºC before opening the furnace to cool back to room temperature. To form single layer heterostructures, it was found that the hotplate should be turned to 250 ºC as the cooling process begins.

Characterization of the MoS_2/WS_2 structures created was done via optical microscopy, Raman microscopy, AFM, photoluminescence spectroscopy (PL), SEM and transmission electron microscopy (TEM).

Results and Discussion

The inset in Figure 25 shows a heterostructure's optical contrast within the same triangular island. The differentiation between the two materials was first confirmed by Raman spectroscopy. Figure 25 shows the Raman spectra of the areas highlighted in the insert. The middle island is MoS_2 and the outer island is WS_2. Raman also confirmed single layer MoS_2 to be present because the difference between the E_{2g}^1 peak and A_{1g} peak was ~19 cm^{-1}. Similarly, the single layer WS_2 was also confirmed with 532 nm the

peak at 351 cm^{-1}, which should have had a higher intensity than the peak at 417 cm^{-1}. Raman maps were also created of several samples showing the major peak for MoS_2 at 403 cm^{-1} and WS_2 at 351 cm^{-1}. Many of the maps created show similar results to the Figure 26 shown below where the MoS_2 is the predominant species while WS_2 is primarily seen along the edges. In some cases, though, WS_2 can be seen in the center of the MoS_2, marking the growth of a second monolayer of WS_2 on top of the MoS_2.

To confirm that the Raman spectrum for these heterostructures is a result of the individual materials and that the new structure is not interfering with the vibrational frequencies, AFM was also done to confirm the number of layers. As can be observed from Figure 28, the height profile across the center structure like the one shown in Figure 27 has very little to no change present when moving from the center to the outside. While there should be some height discrepancy between the two different materials, it is not easily seen in AFM because the single layer heights are so similar, MoS_2 being 0.7 nm and WS_2 being 0.8 nm.

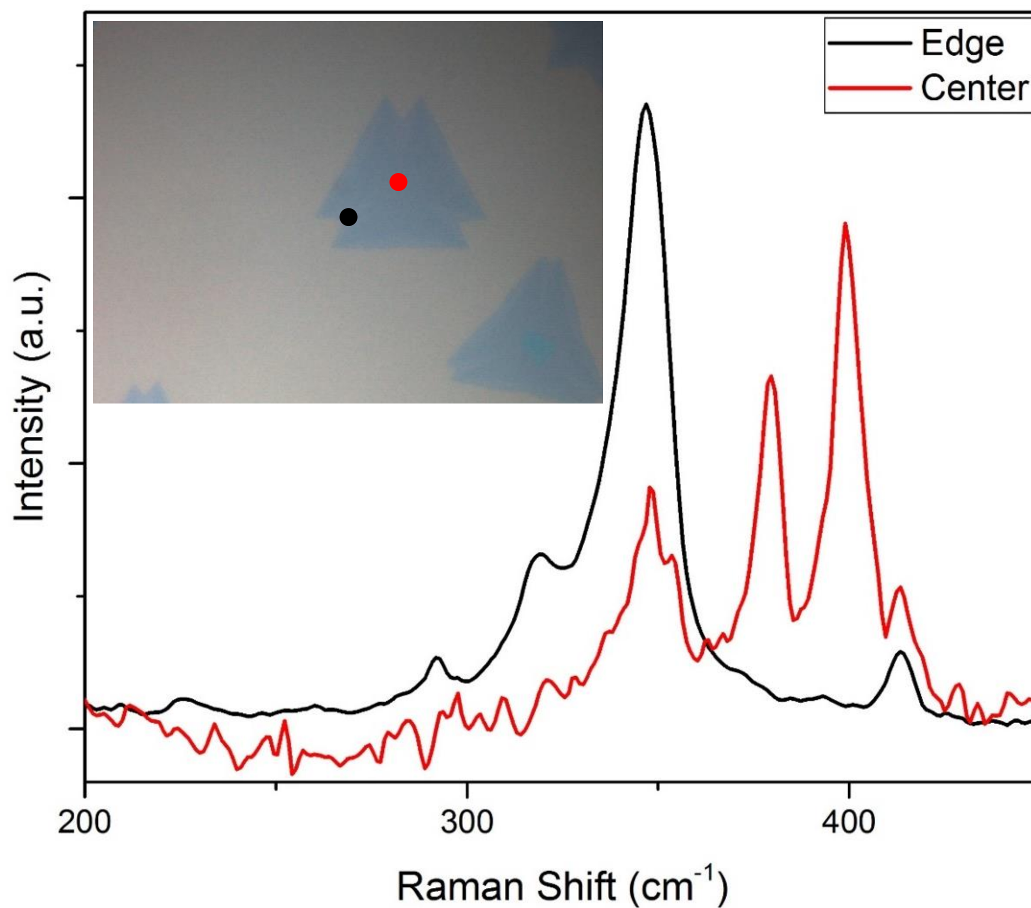

Figure 26 Raman of the optical image from the inset. The black dot corresponds to the Raman shown in black confirming growth of WS_2.The red dot corresponds to the Raman shown in red confirming growth of MoS_2.

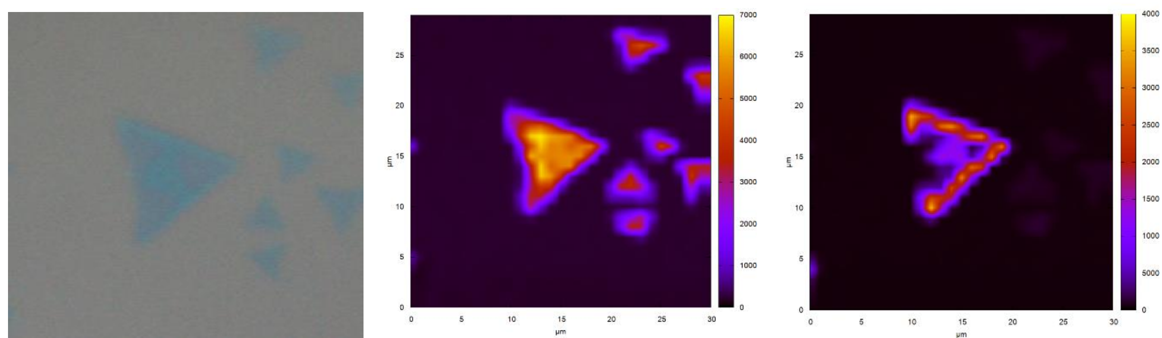

Figure 27 Optical image of a heterostrucutre (left). Raman maps taken of the sample from the left panel. Raman map of MoS_2 recorded at 403 cm^{-1} (middle) and Raman map of WS_2 recorded at 351 cm^{-1} (right).

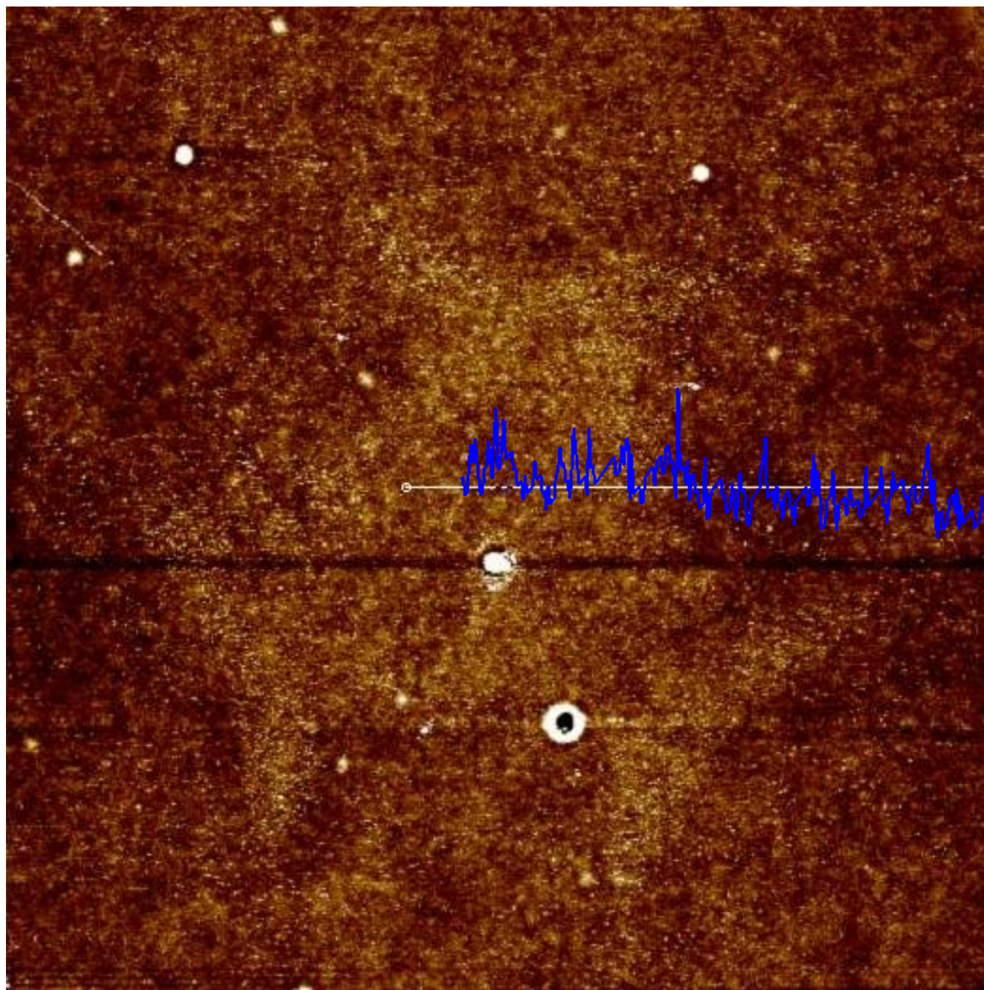

Figure 28 AFM from the center region to the outer region similar to the flake shown in Figure 25 showing no discernable change in the height between the two structures.

PL of a similar area mapped by Raman is shown in Figure 29 for comparison of the excitation. The outside of the islands appears brighter because the Cy5 filter cube being used gives a better excitation of the WS_2 wavelength, making the MoS_2 in the center appear dark. There is also a brighter area around the area that the two interfaces meet, most likely due to higher electron density in these areas.

Electrical properties of the vertical species have been investigated thoroughly using traditional FETs,[108] femtosecond pump-probe spectroscopy,[109] and Kelvin probe force microscopy (KPFM)[107] to observe interaction between van der Waals layers but little work has been done thus far as to investigate the changes in electrical properties due to the change as electrons flow laterally electron flow between the two. We present a concept of how to measure the current through just MoS_2, how it changes when flowing through both MoS_2 and WS_2, and finally how it changes when flowing through WS_2 with a center portion of MoS_2 separating two sides of WS_2. The first device created is shown in Figure 30, but the results of this experiment have been inconclusive thus far. The problems previously observed in synthesis of WS_2, where a large leakage current is present, gives little validity to the current results most likely due to the extreme conditions used in the synthesis process. The materials need to be transferred to a different substrate for device fabrication, like in case of WS_2 from Chapter 2. This should eliminate the leakage current. This will leave an avenue for future work beyond what has already been presented here.

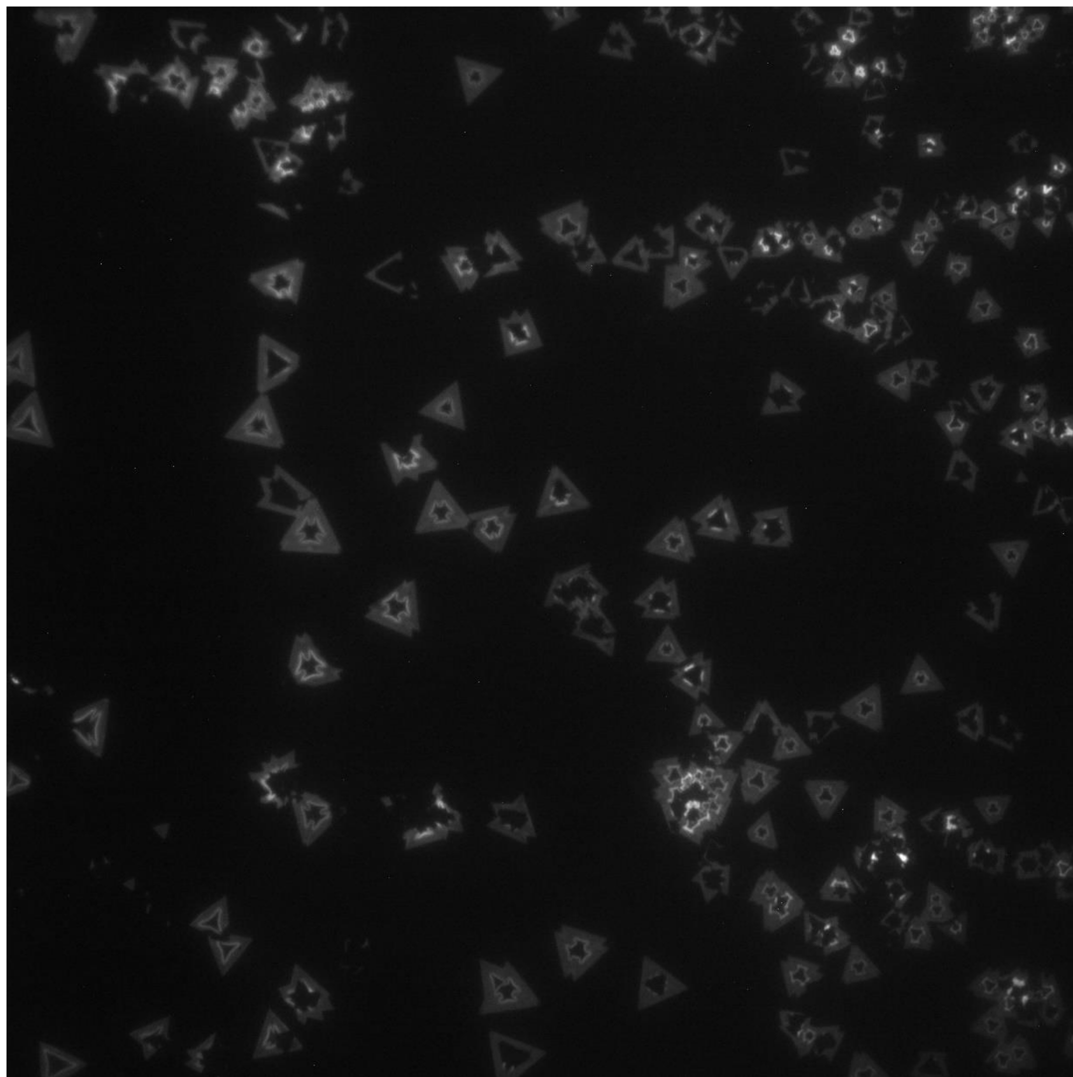

Figure 29 PL map of the same sample shown in Figure 27.

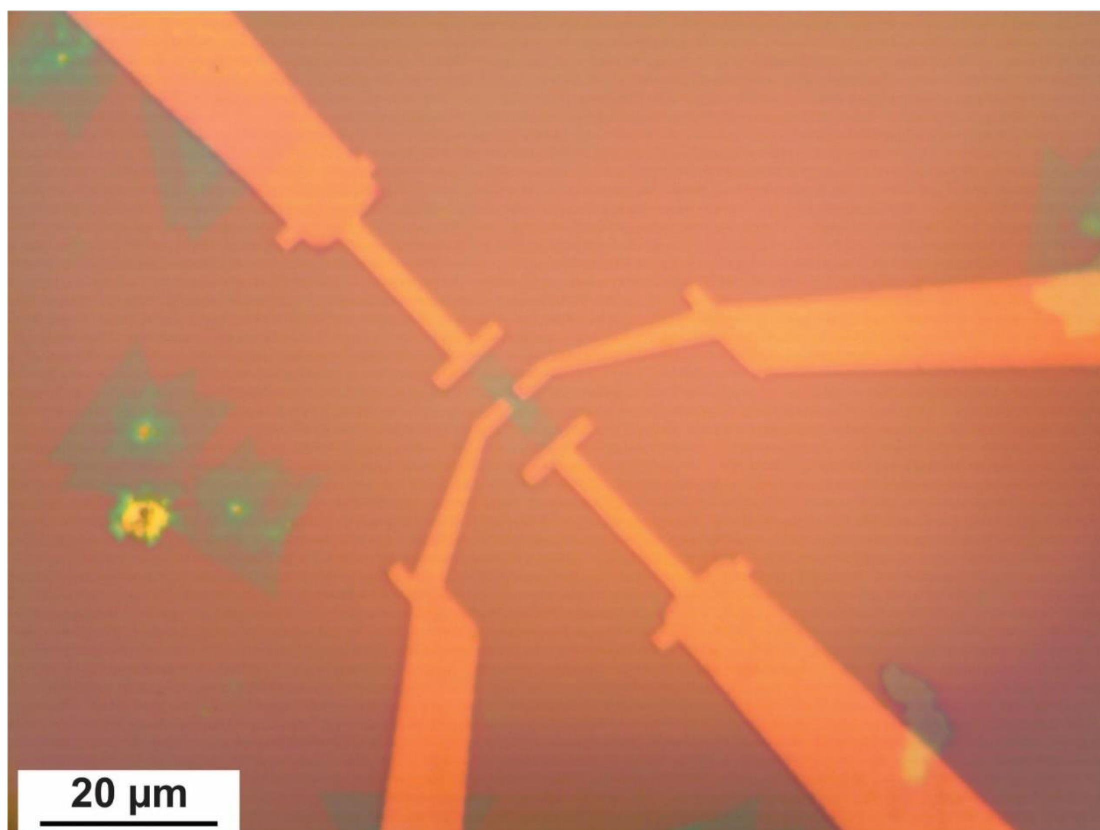

Figure 30 Primary attempt at measuring electronic properties of an in-plane MoS_2/WS_2 heterostructure device.

Conclusion and Future Outlook

TMDs continue to be explored as complementary materials to graphene for a variety of applications. There is also a growing interest in emerging heterostructures of 2D materials, which provide a more customizable way to design electronic properties. It has been discussed here that monolayer, bilayer and trilayer MoS_2 still have properties to be explored and even more when placed onto the surface of another material. Alterations to these materials could also prove useful, such as functionalization.

Much work still needs to be done to further improve CVD of WS_2, as has been done for MoS_2 before it. We have shown a potential increase in the mobility compared to current standards than have been produced. The development of WS_2 could very easily follow the same trend as MoS_2 with its next step being the development of CVD procedures for bilayer and trilayer materials to determine if the same trend can be observed. Regardless of how the few layered materials behave, it could prove even more useful to place and/or grow WS_2 on other materials, such as boron nitride, to further enhance the mobility, or possibly other properties as well. The combination of the two materials, MoS_2 and WS_2 in the same plane could tailor electrical and optical properties in much more specific ways than seen placing one atop of the other.

While TMDs enjoy the increasing popularity, there may still be some novelty left to explore graphene in different heterostructures. In this work, graphene has been laid upon boron nitride to boost its already amazing electronic properties. It was also shown that the exact same graphene flake, does have better properties when placed onto boron

nitride. In the future work, a graphene flake on two different substrates can then be functionalized to help accurately determine shifts in the Dirac point caused by different functional groups.

References

1. Lee, C., Wei, X., Kysar, J. W. & Hone, J. Measurement of the elastic properties and intrinsic strength of monolayer graphene. *Science* **321,** 385–388 (2008).

2. Eda, G., Fanchini, G. & Chhowalla, M. Large-area ultrathin films of reduced graphene oxide as a transparent and flexible electronic material. *Nat. Nanotechnol.* **3,** 270–274 (2008).

3. Castro-Neto, A. H., Peres, N. M. R., Novoselov, K. S. & Geim, A. K. The electronic properties of graphene. *Rev. Mod. Phys.* **81,** 109–162 (2009).

4. Chen, J. H., Jang, C., Xiao, S., Ishigami, M. & Fuhrer, M. S. Intrinsic and extrinsic performance limits of graphene devices on SiO2. *Nat. Nanotechnol.* **3,** 206–209 (2008).

5. Xia, F., Farmer, D. B., Lin, Y. M. & Avouris, P. Graphene field-effect transistors with high on/off current ratio and large transport band gap at room temperature. *Nano Lett.* **10,** 715–718 (2010).

6. Stankovich, S. *et al.* Graphene-based composite materials. *Nature* **442,** 282–286 (2006).

7. Reina, A. *et al.* Large-scale pattern growth of graphene films for stretchable transparent electrodes. *Nano Lett.* **9,** 30–35 (2009).

8. Nair, R. R. *et al.* Fine Structure Constant Defines Visual Transperency of Graphene. *Science (80-.).* **320,** 2008 (2008).

9. Orlita, M. *et al.* Approaching the dirac point in high-mobility multilayer epitaxial graphene. *Phys. Rev. Lett.* **101,** 1–5 (2008).

10. Gmitra, M., Konschuh, S., Ertler, C., Ambrosch-Draxl, C. & Fabian, J. Band-structure topologies of graphene: Spin-orbit coupling effects from first principles. *Phys. Rev. B - Condens. Matter Mater. Phys.* **80,** 2–7 (2009).

11. Zhang, Y. B., Tan, Y. W., Stormer, H. L. & Kim, P. Experimental observation of the quantum Hall effect and Berry's phase in graphene. *Nature* **438,** 201–204 (2005).

12. Dean, C. R. *et al.* Boron nitride substrates for high-quality graphene electronics. *Nat. Nanotechnol.* **5,** 722–726 (2010).

13. Lu, J. *et al.* Order–disorder transition in a two-dimensional boron–carbon–nitride alloy. *Nat. Commun.* **4,** 1–7 (2013).

14. R. R. Nair, W. C. Ren, R. Jalil, I. Riaz, V. G. Kravets, L. Britnell, P. Blake, F. Schedin, A. S. Mayorov, S. Yuan, M. I. Katsnelson, H. M. Cheng, W. Strupinski, L. G. Bulusheva, A. V. Okotrub, I. V. Grigorieva, A. N. Grigorenko, K. S. Novoselov, A. K. G. Fluorographene: a Two Dimensional Counterpart of Teflon R. *Small* 1–20 (2010).

15. Park, S. & Ruoff, R. S. Chemical methods for the production of graphenes. *Nat Nano* **4,** 217–224 (2009).

16. Ci, L. *et al.* Atomic layers of hybridized boron nitride and graphene domains. *Nat. Mater.* **9,** 430–435 (2010).

17. Butler, S. Z. *et al.* Progress, challenges, and opportunities in two-dimensional materials beyond graphene. *ACS Nano* **7,** 2898–2926 (2013).

18. Two-dimensional, S. *et al.* Emerging Device Applications for. *ACS Nano* **8,** 1102–1120 (2014).

19. Wang, Q. H., Kalantar-Zadeh, K., Kis, A., Coleman, J. N. & Strano, M. S. Electronics and optoelectronics of two-dimensional transition metal dichalcogenides. *Nat. Nanotechnol.* **7,** 699–712 (2012).

20. Fiori, G. *et al.* Electronics based on two-dimensional materials. *Nat. Nanotechnol.* **9,** 768–779 (2014).

21. Lv, R. *et al.* Transition metal dichalcogenides and beyond: Synthesis, properties, and applications of single- and few-layer nanosheets. *Acc. Chem. Res.* **48,** 56–64 (2015).

22. Kobayashi, K. & Yamauchi, J. Electronic structure and scanning-tunneling-microscopy image of molybdenum dichalcogenide surfaces. *Phys. Rev. B* **51,** 17085–17095 (1995).

23. Ding, Y. *et al.* First principles study of structural, vibrational and electronic properties of graphene-like MX2 (M=Mo, Nb, W, Ta; X=S, Se, Te) monolayers. *Phys. B Condens. Matter* **406,** 2254–2260 (2011).

24. Transactions, I. & Devices, E. Performance Limits of Monolayer Transition Metal Dichalcogenide Transistors. 1–13 (2014). doi:10.1109/TED.2011.2159221

25. Kuc, A., Zibouche, N. & Heine, T. How does quantum confinement influence the electronic structure of transition metal sulfides TmS2. *arXiv:1104.3670* 1–11 (2011). doi:10.1103/PhysRevB.83.245213

26. Schwierz, F. Graphene transistors. *Nat. Publ. Gr.* **5,** 487–496 (2031).

27. Mak, K., Lee, C., Hone, J., Shan, J. & Heinz, T. Atomically Thin MoS_{2}: A New Direct-Gap Semiconductor. *Phys. Rev. Lett.* **105,** 136805 (2010).

28. Zhao, W. *et al.* Evolution of electronic structure in atomically thin sheets of ws 2 and wse2. *ACS Nano* **7,** 791–797 (2013).

29. Zaumseil, J., Baldwin, K. W. & Rogers, J. A. Contact resistance in organic transistors that use source and drain electrodes formed by soft contact lamination. *J. Appl. Phys.* **93,** 6117–6124 (2003).

30. Jena, D. & Konar, A. Enhancement of carrier mobility in semiconductor nanostructures by dielectric engineering. *Phys. Rev. Lett.* **98,** 1–4 (2007).

31. S.V. Morozov, K.S. Novoselov, M.I. Katsnelson, F. Schedin, D.C. Elias, J.A. Jaszczak, A. K. G. Giant Intrinsic Carrier Mobilities in Graphene and Its Bilayer S.V. 4–8

32. RadisavljevicB *et al.* Single-layer MoS2 transistors. *Nat Nano* **6,** 147–150 (2011).

33. Yoon, Y., Ganapathi, K. & Salahuddin, S. How good can monolayer MoS_2 transistors be? *Nano Lett.* **11,** 3768–73 (2011).

34. Wu, W. *et al.* High mobility and high on / off ratio field-effect transistors based on chemical vapor deposited single-crystal MoS 2 grains. *Appl. Phys. Lett.* **102,** 142106

(2013).

35. Late, D. J. *et al.* Sensing behavior of atomically thin-layered MoS2 transistors. *ACS Nano* **7,** 4879–4891 (2013).

36. Lopez-Sanchez, O., Lembke, D., Kayci, M., Radenovic, A. & Kis, A. Ultrasensitive photodetectors based on monolayer MoS2. *Nat. Nanotechnol.* **8,** 497–501 (2013).

37. Lipatov, A., Sharma, P., Gruverman, A., Sinitskii, A. & Alexey Lipatov,† Pankaj Sharma,‡ Alexei Gruverman,‡, and A. S. Optoelectrical Molybdenum Disulfide (MoS2)-Ferroelectric Memories. *Am. Chem. Soc.* **9,** 8089–8098 (2015).

38. Du, G. *et al.* Superior stability and high capacity of restacked molybdenum disulfide as anode material for lithium ion batteries. *Chem. Commun.* **46,** 1106–1108 (2010).

39. Frindt, R. F. Single crystals of MoS2 several molecular layers thick. *J. Appl. Phys.* **37,** 1928–1929 (1966).

40. M, C. Photoluminescence from Chemically Exfoliated MoS2. *Nano Lett.* **12,** 526 (2012).

41. Coleman, J. N. *et al.* Two-Dimensional Nanosheets Produced by Liquid Exfoliation of Layered Materials. *Science (80-.).* **331,** 568–571 (2011).

42. Smith, R. J. *et al.* Large-scale exfoliation of inorganic layered compounds in aqueous surfactant solutions. *Adv. Mater.* **23,** 3944–3948 (2011).

43. Bao, W. *et al.* Visualizing nanoscale excitonic relaxation properties of disordered edges and grain boundaries in monolayer molybdenum disulfide. *Nat. Commun.* **6,** 1–7 (2015).

44. Lee, Y. H. *et al.* Synthesis of large-area MoS2 atomic layers with chemical vapor deposition. *Adv Mater* **24,** 2320–2325 (2012).

45. Najmaei, S. *et al.* Vapor Phase Growth and Grain Boundary Structure of Molybdenum Disulfide Atomic Layers. *arXiv.org* **cond-m,** 754–759 (2013).

46. Lee, Y. *et al.* Synthesis and Transfer of Single Layer Transition Metal Disulfides on Diverse Surfaces Synthesis and Transfer of Single Layer Transition Metal Disulfides on Diverse Surfaces. *Nano Lett.* **13,** 1852–1857 (2013).

47. van der Zande, A. M. *et al.* Grains and grain boundaries in highly crystalline monolayer molybdenum disulphide. *Nat. Mater.* **12,** 554–61 (2013).

48. Wang, S. S. *et al.* Shape Evolution of Monolayer MoS2 Crystals Grown by Chemical Vapor Deposition. *Chem. Mater.* **26,** 6371–6379 (2014).

49. Yu, Y. *et al.* Controlled scalable synthesis of uniform, high-quality monolayer and few-layer MoS2 films. *Sci. Rep.* **3,** 1866 (2013).

50. Liu, Z., Najmaei, S., Zhan, Y., Ajayan, P. M. & Lou, J. Large Area Vapor Phase Growth and 2D Engineering of Atomic Layers. (2012).

51. Wu, S. *et al.* Vapor-solid growth of high optical quality MoS2 monolayers with near-unity valley polarization. *ACS Nano* **7,** 2768–2772 (2013).

52. Liu, B. K., Zhang, W., Lee, Y. & Lin, Y. Supporting Materials Growth of Large-Area and

Highly Crystalline MoS 2 Thin Layers on Insulating Substrates. **2,** 1–9

53. Kang, K. *et al.* High-mobility three-atom-thick semiconducting films with wafer-scale homogeneity. *Nature* **520,** 656–660 (2015).

54. Lin, Z. *et al.* Facile synthesis of MoS2 and MoxW1-xS2 triangular monolayers. *APL Mater.* **2,** 92514 (2014).

55. Lauritsen, J. V. *et al.* Size-dependent structure of MoS2 nanocrystals. *Nat. Nanotechnol.* **2,** 53 (2007).

56. Ming Xia, Bo Li, K. Y., Giovanni Capellini, GangNiu, Yongji Gong, WuZhou, P. M. A. & Xie, and Y.-H. Spectroscopic Signatures of AA0 and AB Stacking of Chemical Vapor Deposited Bilayer MoS2. (2009). doi:10.1007/3-540-35375-5

57. Liu, K. *et al.* Evolution of Interlayer Coupling in Twisted MoS2 Bilayers. *arXiv Prepr. arXiv …* **5,** 1–6 (2014).

58. Shi, Y., Li, H. & Li, L.-J. Recent advances in controlled synthesis of two-dimensional transition metal dichalcogenides via vapour deposition techniques. *Chem. Soc. Rev.* **44,** 2744–56 (2015).

59. Lipatov, A. *et al.* Few-layer titanium trisulfide (TiS3) field-effect transistors. *Nanoscale* 12291–12296 (2015). doi:10.1039/C5NR01895A

60. Li, H. *et al.* From bulk to monolayer MoS 2: Evolution of Raman scattering. *Adv. Funct. Mater.* **22,** 1385–1390 (2012).

61. Lee, C. *et al.* Anomalous lattice vibrations of single-and few-layer MoS2. *ACS Nano* **4,** 2695–700 (2010).

62. Sinitskii, A., Dimiev, A., Kosynkin, D. V. & Tour, J. M. Graphene nanoribbon devices produced by oxidative unzipping of carbon nanotubes. *ACS Nano* **4,** 5405–5413 (2010).

63. Britnell, L. *et al.* Field - effect tunneling transistor based on vertical graphene heterostructures. 1–11

64. Zhang, Y. *et al.* Controlled Growth of High-Quality Monolayer WS 2 Layers on Sapphire. *ACS Nano* **7,** 8963–8971 (2013).

65. Gutierrez, H. R. *et al.* Extraordinary room-temperature photoluminescence in WS2 triangular monolayers. *Nano Lett.* **13,** 3447–3454 (2012).

66. Berkdemir, A. *et al.* Identification of individual and few layers of WS2 using Raman spectroscopy. *Sci. Rep.* **3,** 1755 (2013).

67. Lan, C., Li, C., Yin, Y. & Liu, Y. Large-area synthesis of monolayer WS 2 and its ambient-sensitive photo-detecting performance. *Nanoscale* **7,** 5974–5980 (2015).

68. Hwang, W. S. *et al.* Transistors with chemically synthesized layered semiconductor WS2 exhibiting 10^5 room temperature modulation and ambipolar behabvior. *Appl. Phys. Lett.* **13107,** 101 (2012).

69. Song, J. *et al.* Conformal Synthesis of Tungsten Disul fi de Nanosheets Using Atomic Layer Deposition. *ACS Nano* **7,** 11333–11340 (2013).

70. Physics, E. & Engineering, I. High Performance Field-Effect Transistor Based on Multilayer Tungsten Disulfide Xue Liu † ¶ , Jin Hu † ¶ , Chunlei Yue † , Della Fera, Nicholas D † , Yun Ling ‡§ , Zhiqiang Mao † , Jiang Wei † * † ‡.

71. Geim, A. K. & Grigorieva, I. V. Van der Waals heterostructures. *Nature* **499,** 419–425 (2014).

72. Li, H. *et al.* A Universal, Rapid Method for Clean Transfer of Nanostructures onto Various Substrates. *ACS Nano* **8,** 6563–6570 (2014).

73. Woods, C., Britnell, L. & Eckmann, A. Commensurate-incommensurate transition for graphene on hexagonal boron nitride. *arXiv Prepr. arXiv …* (2014).

74. Withers, F. *et al.* Light-emitting diodes by band-structure engineering in van der Waals heterostructures. *Nat Mater* **14,** 301–306 (2015).

75. Wang, L. *et al.* One-dimensional electrical contact to a two-dimensional material. *Science (80-.).* **342,** 614–7 (2013).

76. Kretinin, A. V *et al.* Electronic properties of graphene encapsulated with different 2D atomic crystals. *Nano Lett.* 1–19 (2014). doi:10.1021/nl5006542

77. Ambacher, O. *et al.* Two-dimensional electron gases induced by spontaneous and piezoelectric polarization charges in N- and Ga-face AlGaN/GaN heterostructures. *J. Appl. Phys.* **85,** 3222 (1999).

78. J. Wang, J. B. Neaton, H. Zheng, V. Nagarajan, S. B. Ogale, D. Viehland, V.Venugopalan, D.G. Schlom, U. V.Waghmare, N. A. Hill, and K.M. Rabe, M.Wuttig, and R. R. Epitaxial BiFeO3Multiferroic Thin FilmHeterostructures. (2003).

79. Duan, X. F. & Lieber, C. M. General synthesis of compound semiconductor nanowires. *Adv. Mater.* **12,** 298–302 (2000).

80. Lauhon, L. J., Gudiksen, M. S., Wang, D. & Lieber, C. M. Epitaxial core-shell and core-multishell nanowire heterostructures. *Nature* **420,** 57–61 (2002).

81. Tan, L. K. *et al.* Atomic layer deposition of a MoS_2 film. *Nanoscale* **6,** 10584–8 (2014).

82. Huang, C. *et al.* Lateral heterojunctions within monolayer MoSe2–WSe2 semiconductors. *Nat. Mater.* **13,** 1–6 (2014).

83. Kibsgaard, J., Chen, Z., Reinecke, B. N. & Jaramillo, T. F. Engineering the surface structure of MoS2 to preferentially expose active edge sites for electrocatalysis. *Nat. Mater.* **11,** 963–969 (2012).

84. Chen, J. H. *et al.* Printed graphene circuits. *Adv. Mater.* **19,** 3623–3627 (2007).

85. Kim, K. K. K. K. K. *et al.* Synthesis and Characterization of Hexagonal Boron Nitride Film as a Dielectric Layer for Graphene Devices. *ACS Nano* **6,** 8583–8590 (2012).

86. Liang, X. *et al.* Toward clean and crackless transfer of graphene. *ACS Nano* **5,** 9144–9153 (2011).

87. Ma, Y., Dai, Y., Guo, M., Niu, C. & Huang, B. Graphene adhesion on MoS2 monolayer: An ab initio study. *Nanoscale* **3,** 3883–3887 (2011).

88. Shi, Y. *et al.* van der Waals Epitaxy of MoS 2 Layers Using Graphene As Growth Templates. *Nano Lett.* **12,** 2784–2791 (2012).

89. Giovannetti, G., Khomyakov, P. A., Brocks, G., Kelly, P. J. & Brink, J. Van Den. Substrate-induced bandgap in graphene on hexagonal boron nitride. *Phys. Rev. B* **76,** 73103 (2007).

90. Zomer, P. J., Dash, S. P., Tombros, N. & van Wees, B. J. A new transfer technique for high mobility graphene devices on commercially available hexagonal boron nitride. 10–12 (2011). doi:10.1063/1.3665405

91. Huang, Y. *et al.* Reliable Exfoliation of Large-Area High-Quality Flakes of Graphene and Other Two-Dimensional Materials. *ACS Nano* **9,** 10612–10620 (2015).

92. Ferrari, A. C. *et al.* Raman spectrum of graphene and graphene layers. *Phys. Rev. Lett.* **97,** 1–4 (2006).

93. Ferrari, A. C. & Basko, D. M. Raman spectroscopy as a versatile tool for studying the properties of graphene. *Nat Nanotechnol* **8,** 235–246 (2013).

94. Graf, D. & Ensslin, K. Spatially Resolved Raman Spectroscopy of Single- and Few-Layer Graphene. *Solid State Phys.* 1–6 (2008). doi:10.1021/nl061702a

95. Mohiuddin, T. M. G. *et al.* Uniaxial strain in graphene by Raman spectroscopy: G peak splitting, Grüneisen parameters, and sample orientation. *Phys. Rev. B - Condens. Matter Mater. Phys.* **79,** (2009).

96. R. V. Gorbachev, I. Riaz, R. R. Nair, R. Jalil, L. Britnell, B. D. Belle, E. W. Hill, K. S. Novoselov, K. Watanabe, T. Taniguchi, A. K. Geim, P. B. Hunting for Monolayer Boron Nitride: Optical and Raman Signatures R. *Harvard Bus. Sch. Cases* 1 (2010). doi:10.1002/smll.201001628

97. Levendorf, M. P. *et al.* Graphene and boron nitride lateral heterostructures for atomically thin circuitry. *Nature* **488,** 627–632 (2012).

98. Gong, Y. *et al.* Vertical and in-plane heterostructures from WS2/MoS2 monolayers. *Nat Mater* **13,** 1135–1142 (2014).

99. Oostinga, J. B., Heersche, H. B., Liu, X., Morpurgo, A. F. & Vandersypen, L. M. K. Gate-induced insulating state in bilayer graphene devices. *Nat. Mater.* **7,** 151–157 (2008).

100. Hyun Jeong, S. B., Hye Min Oh, Hyeon Jun Jeong, Sung-Jin An, G. H. H., Kim, H. & Ki Kang Kim, Jin Cheol Park, Young Hee Lee, Gilles Lerondel, and M. S. J. Semiconductor-Insulator- Semiconductor Diode Consisting of Monolayer MoS2,h-BN, and GaN Heterostructure. 10032–10038 (2015). doi:10.1021/acsnano.5b04233

101. Lee, G.-H. *et al.* Flexible and Transparent MoS 2 Field-Effect Transistors on Hexagonal Boron Nitride-Graphene Heterostructures. *ACS Nano* **7,** 7931–7936 (2013).

102. Lee, G.-H. *et al.* Highly Stable, Dual-Gated MoS 2 Transistors Encapsulated by Hexagonal Boron Nitride with Gate-Controllable Contact, Resistance, and Threshold Voltage. *ACS Nano* **9,** 7019–7026 (2015).

103. Wang, L. *et al.* Monolayer hexagonal boron nitride films with large domain size and clean interface for enhancing the mobility of graphene-based field-effect transistors. *Adv.*

Mater. **26,** 1559–1564 (2014).

104. Ruzmetov, D. *et al.* Vertical 2D/3D Semiconductor Heterostructures Based on Epitaxial Molybdenum Disulfide and Gallium Nitride. *ACS Nano* **10,** 3580–3588 (2016).

105. Okada, M. *et al.* Direct chemical vapor deposition growth of WS2 atomic layers on hexagonal boron nitride. *ACS Nano* **8,** 8273–8277 (2014).

106. Yu, Y. *et al.* Equally Efficient Interlayer Exciton Relaxation and Improved Absorption in Epitaxial and Non-epitaxial MoS2 / WS2 Heterostructures Equally Efficient Interlayer Exciton Relaxation and Improved Absorption in Epitaxial and Non-epitaxial MoS 2 / WS 2 Heterost. *Nano Lett.* **15,** 4 (2015).

107. Chen, K. *et al.* Electronic Properties of MoS2-WS2 Heterostructures Synthesized with Two-Step Lateral Epitaxial Strategy. *ACS Nano* 9868–9876 (2015). doi:10.1021/acsnano.5b03188

108. Huo, N. *et al.* Novel and enhanced optoelectronic performances of multilayer MoS2 -WS2 heterostructure transistors. *Adv. Funct. Mater.* **24,** 7025–7031 (2014).

109. Hong, X. *et al.* Ultrafast charge transfer in atomically thin MoS2/WS2 heterostructures. *Nat. Nanotechnol.* **9,** 1–5 (2014).

110. Koåmider, K. & Fernández-Rossier, J. Electronic properties of the MoS2-WS2 heterojunction. *Phys. Rev. B - Condens. Matter Mater. Phys.* **87,** 41–44 (2013).

111. Zhang, X. Q., Lin, C. H., Tseng, Y. W., Huang, K. H. & Lee, Y. H. Synthesis of lateral heterostructures of semiconducting atomic layers. *Nano Lett.* **15,** 410–415 (2015).

112. Duan, X. *et al.* Lateral epitaxial growth of two-dimensional layered semiconductor heterojunctions. *Nat Nanotechnol* **9,** 1024–1030 (2014).